ORIGINAL PAPER



Variable-order approach to nonlocal elasticity: theoretical formulation, order identification via deep learning, and applications

Received: 22 February 2021 / Accepted: 5 September 2021 © The Author(s), under exclusive licence to Springer-Verlag GmbH Germany, part of Springer Nature 2021

Abstract

This study presents the formulation of the variable-order continuum mechanics theory and its application to the analysis of nonlocal heterogeneous solids. The variable-order continuum theory enables a unique approach to model the response of solids exhibiting position-dependent nonlocal behavior. The formulation also guarantees frame-invariance provided that proper constraints on the functional definition of the variable-order are imposed. The study also presents a deep learning approach to identify the variable-order distribution describing the behavior of the medium. This methodology presents a very promising route for the practical application of the variable-order theory to real-world problems, especially when the microstructure is not known *a priori* and must be inferred from the physical response of the medium. The capabilities of the variable-order theory are illustrated by numerically simulating the static response of nonlocal beams having either a porous or a functionally graded core. The reduced-order variable fractional model shows excellent accuracy and significant computational efficiency when compared with a reference solution produced by a 3D finite element model that fully resolves the beam geometry.

Keywords Variable-order fractional calculus · Nonlocal elasticity · Deep learning · Porous structures · Functionally graded structures

1 Introduction

In recent years, fractional calculus has emerged as a powerful mathematical tool to model a variety of complex physical phenomena. Fractional-order operators allow for differentiating and integrating a function to any real or complex order, are intrinsically multiscale, and provide a natural way to account for several complex physical mechanisms in the analysis of continua such as, for example, nonlocal effects, medium heterogeneity, and memory effects. These characteristics of fractional operators have led to a surge of interest in fractional calculus and its application to the simulation of several physical problems. Some of the areas that have seen the largest number of applications include model-order reduction [1,2], formulation of constitutive equations for viscoelastic

 ☑ Fabio Semperlotti fsemperl@purdue.edu Mehdi Jokar

mjokar@purdue.edu

Published online: 27 September 2021

School of Mechanical Engineering, Ray W. Herrick Laboratories, Purdue University, West Lafayette, IN 47907, USA materials [3,4], modeling of anomalous and hybrid transport in complex materials [5–10], modeling of nonlocal elasticity and size-dependent effects [10–19], and homogenization of heterogeneous structures [2,10,20]. These applications have highlighted the ability of fractional calculus to capture and accurately model the response of advanced materials. The interested reader can find a detailed review focusing on the application of fractional calculus to the characterization and modeling of complex materials in [21].

The modeling of nonlocal and heterogeneous media is one of the areas that has seen a significant acceleration in the use of fractional-order operators. Several researchers have demonstrated the advantages of using space-fractional continuum formulations in the modeling of nonlocal elasticity [11–14] as well as the homogenization of heterogeneous structures [2,10,20]. In the context of nonlocal elasticity, fractional calculus has enabled the formulation of self-adjoint, positive-definite and well-posed formulations enabling consistent predictions free from boundary effects [11,12]. This latter aspect contrasts with classical integral approaches to nonlocal elasticity where it is not always possible to achieve a self-adjoint formulation and additional constitutive boundary conditions



are essential to ensure a well-posed form of the governing equations [22,23]. More recently, fractional calculus has also been used to combine selected characteristics of nonlocal elasticity, typical of classical integral and gradient formulations. The resulting formulation captures both stiffening and softening effects in a unified and stable manner, free from boundary effects [24]. Finally, space-fractional operators have been used to develop homogenization approaches capable of modeling the dynamic behavior of periodic structures beyond the classical long-wavelength limit, and hence capable of capturing the occurrence of frequency band-gaps [20].

All the above mentioned applications have typically used constant-order (CO) fractional models. Although the constant-order fractional calculus (CO-FC) formalism is capable of capturing several important physical mechanisms, it does not apply to those classes of physical phenomena whose order is variable and function of other physical parameters. An example of a system that is well described by variable-order (VO) operators consists in the reaction kinetics of proteins. This process was shown to exhibit relaxation mechanisms that are properly described by a temperaturedependent fractional-order [25]. Another relevant example, includes the response of amorphous and viscoelastic materials where it has been shown that the stress-strain constitutive relation exhibits a fractional-order behaviour that could be described accurately by using either a strain-dependent or a time-dependent variable fractional-order [26–28]. These examples represent a small subset of the many different physical phenomena that are characterized by evolving properties and that can be described efficiently by VO fractional operators.

Variable-order operators can be seen as a natural extension of CO operators and were defined by Samko et al. in 1993 [29]. In VO operators, the order can vary either as a function of dependent or independent variables of integration or differentiation such as, time, space, or even of external variables (e.g. temperature or external forcing conditions). As the variable-order fractional calculus (VO-FC) formalism allows updating the system's order depending on either its instantaneous or historical response, the corresponding model can evolve seamlessly to describe widely dissimilar dynamics without the need to modify the structure of the underlying governing equations. Thus, a very significant feature of VObased physical models consists in their evolutionary nature, which can play a critical role in the simulation of nonlinear systems [30–32]. In recent years, many applications of VO-FC to practical real-world problems have been explored including, but not limited to, the response of nonlinear oscillators with spatially varying constitutive law for damping [31,32], complex nonlinear dynamics [31–34], and modeling of anomalous diffusion in complex structures with spatially and temporally varying properties [35,36]. The interested reader can find a comprehensive review of applications in [37].

In the context of material modeling, several researchers have leveraged the evolutionary property of VO operators to model a variety of physical phenomena such as structural damage [38,39], viscoelasticity [26–28], and creep [40]. All of the above mentioned studies have focused on the use of time-fractional VO operators to model different problems. A thorough review of the literature suggests that the development of space-fractional VO continuum mechanics formulations and their use for material modeling is still lacking. Recall that one of the most significant application of space-fractional operators is the modeling of nonlocal elastic behavior. Building on the rapid progress made in the modeling of nonlocal elasticity via CO fractional operators [10–16], we explore in detail the additional modeling capabilities enabled by the application of VO fractional operators.

1.1 Major contributions of the study

Broadly speaking, the present study provides four major contributions. The primary contribution consists in the development of a variable-order space-fractional continuum model capable of capturing heterogeneous nonlocality. The model builds and extends from its CO counterpart presented in [10]. Important aspects such as the acceptable functional variations of the VO are analyzed from the perspective of frame-invariance. We show that, the use of VO operators with no order-memory ensures frame-invariance unconditionally, while the use of weak order-memory and strong order-memory, more likely, renders the formulation non frame-invariant. We merely note that, the use of weak ordermemory operators, particularly in dynamic systems, could lead to a nonphysical ramping up or accumulation of the system energy [30]. Further, we discuss the physical significance of the spatially varying order and relate it to the varying strength of long-range interactions in a nonlocal solid.

The second contribution of this study consists in using the VO space-fractional continuum model to develop a VO analogue of the Euler-Bernoulli beam theory. The VO governing equations for the nonlocal beam are derived in a strong form using variational principles. More specifically, the governing equations are derived by minimization of the total potential energy of the beam. Additionally, we show that the VO modeling of the nonlocal beam results in a self-adjoint system with a quadratic potential energy, irrespective of the boundary conditions. Consequently, the VO governing equations are well-posed and admit a unique solution, free from boundary effects. This result is in sharp contrast with classical integral nonlocal methods where it is not always possible to achieve a well-posed formulation with quadratic potential energy density.



The third contribution of this work consists in the development of a deep learning based methodology to identify the spatial distribution of VO from the measured response of the system. This approach is possible due to the wellposed nature of the VO approach; a specific characteristic of the fractional-order kinematic approach to nonlocality [11]. We show that bidirectional recurrent neural networks (BRNN) [41] provide an excellent basis to compute the variable fractional-order starting from the deformation field of the nonlocal beam. This approach leverages the computational efficiency of the trained neural network to overcome the computational cost typical of identification approaches that rely on iterative optimization algorithms and cumbersome numerical simulations [42,43]. Among the various neural network architectures, BRNNs were selected due to their internal structure which makes them suitable for boundary value problems. More specifically, a BRNN consists of two sets of recurrent neural networks (RNN) that process the sequential input in opposite directions and where each RNN is capable of learning a sequential behavior corresponding to an independent variable [44,45]. Hence, the BRNN output accounts for the information from past (backward) and future (forward) input states simultaneously, which is consistent with the spatial and nonlocal nature of the problem considered in this study. We will discuss this aspect in detail in Sect. 4.2.

In regards to the above discussion, we note that researchers have employed physics informed neural networks [46], that are deep, fully connected, and feed forward networks, to solve the inverse problem consisting in the determination of the order characterising turbulent flows [47,48]. While this solution technique achieves a high accuracy without requiring a large training set, the price to pay is the computational cost of training a network for every problem the network is requested to solve. On the contrary, we will show that the our proposed method can accurately solve problems with VO patterns inconsistent with the training data, that is the patterns have never been presented to the network during the training phase. Further, we also demonstrate the ability of the proposed network to predict closely the trends in the VO, even in the presence of noise in the measured response. Both the aforementioned aspects demonstrate that BRNNs are highly capable of learning the static response of the beam and are generalized enough to solve similar complex and spatially varying nonlocal inverse problems (both in theoretical and in real-world settings).

The final major contribution of this work consists in showing the practical advantages of the VO space-fractional approach over classical integer-order (IO) approaches. Specific examples of significant practical relevance involves the static structural response of either porous or functionally graded beams. For the case of porous beams, we compare the predictions obtained via the VO approach with either

the solution of a high fidelity 3D finite element model (obtained via COMSOL Multiphysics) or of a traditional integer-order (IO) beam model. For the case of functionally graded beams, the predictions of the VO approach are only compared with those of the finite element model. Indeed, theoretical inconsistencies in existing IO approaches for functionally graded beams prevent them to be used for comparison [11,49]. Results demonstrate that the VO approach achieves superior accuracy when compared with classical IO approaches, and significant computational efficiency when compared with 3D finite element approaches.

1.2 Broader relevance of the study

The evolutionary nature of VO operators has drastically expanded the range of opportunities to apply FC to material modeling, particularly in those cases where the underlying physical response of the material evolves significantly in time, space, or as a function of an external stimulus. Experiments have shown that properties of polymers, ductile metals, and rocks evolve across strain hardening and softening regimes depending on their internal microstructure and applied strain rates. In a series of papers, Meng et al. [26,27] have shown that VO models can accurately capture these transitions in the response of polymers and metals. VO-FC has also been used in the modeling of creep in rocks [40], response of viscoelastic materials [28] and dynamics of shape-memory polymers [50]. In all these works, it was shown that VO-FC models admit fewer parameters than the existing models, and the evolution of the mechanical property is well captured by the VO. Patnaik et al. [32,33] have also modeled these transitions in material response using a physics-driven simulation strategy that leverages the peculiar properties of the VO Riemann-Liouville derivative of a constant. This approach was also extended to model the propagation of edge dislocations in lattice structures [38] and dynamic fracture mechanics [39]. All the aforementioned studies demonstrated how the evolution of the VO operators in time, guided by either data-driven or physicsdriven VO laws of variation, provided an extremely powerful approach to capture the rapidly changing physics of the process.

While the above mentioned studies have produced exciting results, as also mentioned previously in this introduction, they have primarily focused on applications of time-fractional VO operators to time-evolving systems. A dual class of problems consists of systems whose response and the underlying physics evolve with space. Consider, as an example, the response of a nonlocal material exhibiting a spatially varying strength of the long-range interactions resulting, as an example, due to either spatial variations in the microstructure or thermal gradients. Other examples can include materials with spatially varying energy



dissipation mechanisms or materials subject to internal processes (e.g. chemical) driven by spatial varying external loads (e.g. thermal). The existing IO (classical) or CO (fractional) approaches to nonlocal elasticity are unable to accurately capture these phenomena, because the strength of the nonlocal attenuation function in these formulations is constant in space. This technical gap is addressed by the VO approach to nonlocal elasticity which is expected to model the response of nonlocal systems exhibiting a spatially varying strength of long-range interactions. In the Sect. 2, we will develop the underlying theory for VO approach to nonlocal elasticity with a spatially varying order law, and we will discuss how the spatially varying order law can be leveraged to account for the spatially varying strength of long-range interactions in complex materials.

The previous discussion highlighted different practical cases that could give rise to a VO space-fractional formulation. However, the order variation cannot always be determined based on fundamental principles. Indeed, while Patnaik et al. [32,33] showed that physics-based order variations are possible and extremely powerful, Meng et al. [26,27] used data fitting to recover the VO behavior from experimental measurements. It is not hard to envision that practical applications might require, and even benefit from, a combination of these two approaches. In fact, bringing this reasoning a step further, one could envision a two-pronged procedure to enable physics-driven VO modeling of a material during the design phase, and a data-driven update of the VO laws (based on measurements) during the operating life. The data-driven approach could enable capturing subtle aspects connected to the actual usage of the material and their impact on its structural behavior. This general perspective motivated us to explore the application of deep learning techniques, in order to determine the feasibility of extracting information relevant to the characterization of the VO from available response data. Indeed, the deep learning technique enabled a direct application of the VO theory to the static analysis of porous and functionally graded beams in Sect. 6. These examples illustrate the significant potential of the VO theory to achieve accurate solutions for complex structural problems in a computationally efficient manner.

The remainder of the paper is structured as follows: first, we present the VO space-fractional continuum model for nonlocal solids. We use the VO model to develop the fractional-order Euler-Bernoulli theory applicable to the analysis of heterogeneously nonlocal beams. Next, we describe the network-based order estimation procedure and illustrate its accuracy by applying to the solution of a set of sample problems. Finally, we present the application of the VO model to the static analysis of porous and functionally graded beams.



2 Variable-order nonlocal continuum theory

In this section, we develop the VO approach to nonlocal elasticity by extending the CO fractional framework [10–16]. For this purpose, we select the fractional-order kinematic approach [10,24] as basis for the VO framework. Although other choices would be possible (such as formulations based on fractional-order stress-strain relations [13,14] or fractional-order strain-displacement relations [15,17]), this approach enables the development of positive-definite and well-posed nonlocal models that are critical for practical applications to systems with general geometry and boundary conditions [11]. The detailed physical interpretation of the fractional-order kinematic approach can be found in [10,12,24].

In the fractional-order kinematic approach, nonlocality is modeled using a fractional-order deformation gradient tensor that relates the differential line elements within the deformed and undeformed configurations. The constitutive modeling, including the definition of strain and stress fields in the nonlocal medium, are analogous to the constant fractional-order kinematic approach to nonlocal elasticity, the details of which can be found in [10,12]. We emphasize that the key principles as well as the derivations conducted in [10,12] also hold true for the VO formulation developed in this study. In other terms, the CO studies conducted in [10,12] can be directly extended to develop the VO formulation by replacing the CO derivatives with the VO derivatives. Hence, in the following, we will only present the key highlights of the VO approach and refer the interested reader to [10,12] for more detailed proofs as well as discussions.

In analogy with the classical strain measures, the nonlocal strain in the fractional-order approach is defined using the difference of the scalar product of the nonlocal fractional-order differential line elements in the deformed and undeformed configurations [10]. Following the detailed procedure outlined in [10], the expression for the VO infinitesimal strain tensor is obtained as:

$$\boldsymbol{\varepsilon} = \frac{1}{2} \left[\nabla^{\alpha(\boldsymbol{x})} \boldsymbol{u} + \nabla^{\alpha(\boldsymbol{x})} \boldsymbol{u}^T \right] \tag{1}$$

where \boldsymbol{u} denotes the displacement field as illustrated in Fig. 1a. In the above equation, $\nabla^{\alpha(\boldsymbol{x})}\boldsymbol{u}$ is the VO fractional gradient given by $(\nabla^{\alpha(\boldsymbol{x})}\boldsymbol{u})_{ij} = D_{x_j}^{\alpha(x)}u_i$. The VO space-fractional derivative $D_{x_j}^{\alpha(x)}u_i$ is taken according to a variable-order Riesz-Caputo (VO-RC) definition with order $\alpha(\boldsymbol{x}) \in (0,1)$ defined on the interval $x_j \in (x_j^-, x_j^+) \subset \mathcal{R}$ and is given by:

$$D_{x_j}^{\alpha(x)} u_i = \frac{1}{2} \Gamma(2 - \alpha(x)) \left[\left[l_{-j}(x) \right]^{\alpha(x) - 1} \right]_{x_j}^{C} D_{x_j}^{\alpha(x)} u_i$$

$$-\left[l_{+j}(\mathbf{x})\right]^{\alpha(\mathbf{x})-1} \quad {}^{C}_{x_{j}}D^{\alpha(\mathbf{x})}_{x_{j}^{+}}u_{i}$$
(2)

where $\Gamma(\cdot)$ is the Gamma function, and $\sum_{x_j}^C D_{x_j}^{\alpha(x)} u_i$ and $\sum_{x_j}^C D_{x_j}^{\alpha(x)} u_i$ are the left- and right-handed VO Caputo derivatives of u_i , respectively. Detailed expressions of the left- and right-handed VO Caputo derivatives are provided in Appendix A. The parameters $l_{-j}(x)$ and $l_{+j}(x)$ are length scales along the jth direction in the deformed configuration. The index j in Eq. (2) is not a repeated index because the length scales are scalar multipliers. In a general scenario, the length scales could be envisioned to be position-dependent, as indicated in Eq. (2). Detailed implications of this assumption are presented later in this section where the physical interpretation of the length scale parameters are discussed. For the sake of brevity, the functional dependence of the length scales on the spatial position will be implied unless explicitly expressed to be a constant.

Further, the stress tensor in the nonlocal isotropic medium is given, analogously to the local case, as:

$$\sigma = \mathbb{C} : \boldsymbol{\varepsilon} \tag{3}$$

where \mathbb{C} denotes the classical fourth-order elasticity tensor. At first glance, the above stress-strain constitutive relation might be deceiving since it maintains the same formal appearance as the classical local counterpart. Although this is a correct statement in principle, in practice, it does not describe the real nature of the relation. Recall that the strain tensor in Eq. (1) was defined via fractional-order derivatives (which are nonlocal in nature), hence the stress defined through the Eq. (3) is nonlocal in nature. Adopting this fractional-order kinematic approach leads to a positive-definite formulation of nonlocal elasticity [11,12,24] which ensures that the resulting governing equations, obtained by minimization of the potential energy, are self-adjoint and mathematically wellposed. We will touch upon this aspect in detail in Sect. 3 by exploring an application to slender beams. Note that all CO fractional continuum relations are recovered when the VO is set to be a constant $\alpha_0 \in (0, 1)$, that is, $\alpha(x) = \alpha_0$. Similarly, all classical (local) continuum mechanics relations are recovered when VO $\alpha(x) = 1, \forall x$.

Before proceeding further, we will first discuss in detail the physical interpretation as well as the implications of the spatially varying length scales and of the VO. From a general perspective, the length scale parameters ensure both the dimensional consistency and the frame-invariance of the formulation. For a frame-invariant model, it is required that the length scales $l_{-j} = x_j - x_j^-$ and $l_{+j} = x_j^+ - x_j$ (see Appendix B). Hence, it follows that the length scales, l_{-j} and l_{+j} , physically denote the dimension of the horizon of nonlocality to the left and to the right of a point x_j along the jth directions.

tion. The length scales have been schematically illustrated in Fig. 1b. The interval of the fractional derivative (x_j^-, x_j^+) defines the horizon of nonlocality along the jth direction, which is schematically shown in Fig. 1b for a generic point $x \in \mathcal{R}^2$. The horizon defines the set of all points in the solid that influence the elastic response at x or, equivalently, the characteristic distance beyond which information of nonlocal interactions is no longer accounted for in the VO fractional derivative. With regards to the latter aspect, the spatially-dependent length scales indicate a spatially varying horizon of nonlocality. The spatial dependence of the horizon of nonlocality can depend on different factors such as, for example, the underlying micro- or macro structure or spatially varying thermal gradients.

Another key aspect of the VO space-fractional formulation in Eq. (2) consists in the introduction of the different length scales $(l_{-}, \text{ and } l_{+})$ which enables the formulation to deal with possible asymmetries in the horizon of nonlocality (e.g. resulting from a truncation of the horizon when approaching a boundary or an interface). More specifically, the different length scales enable an accurate treatment of the frame invariance and ensure a completeness of the kernel in the presence of asymmetric horizons, material boundaries, and interfaces (Fig. 1b). The detailed proof of the completeness of the kernel can be found for a CO fractional formulation in [10]. The same proof directly extends to the VO formulation. To summarize, the asymmetric and spatially varying length scales l_{-} , and l_{+} , allow a definition of the horizon of nonlocality that is capable of capturing the effects of both asymmetries and anisotropies. All these possible cases have been illustrated in Fig. 1b. Clearly, a constant horizon of nonlocality, similar to [10], can be recovered by setting the length scales to be constant functions.

Apart from the spatially variable length scales, the fractional-order formulation also admits the VO as a parameter. In this regard, note that at a given point x, the order $\alpha(x)$ characterizes the strength of the nonlocal interaction on the horizon of nonlocality [10]. The power-law kernel $1/|x|^{\alpha(x)}$ embedded in the definition of the VO fractional derivative is analogous to the attenuation function commonly used in classical integral approaches to nonlocal elasticity. Thus, the VO indicates that the attenuation of the long-range forces and, consequently, the degree of nonlocality vary spatially across the domain of the solid. As an example, consider two points x_1 and x_2 such that $\alpha(x_1) < \alpha(x_2)$. It follows that the degree of nonlocality, (or, in other terms, the strength of long-range interactions) at x_1 is higher than that at x_2 . Note that a higher value of the fractional-order indicates a lower degree of nonlocality [12].

There exist different definitions for the functional variation of the variable fractional-order. These definitions differ in the resulting *order-memory* characteristics of the specific fractional-order operator [30]. The order-memory measures



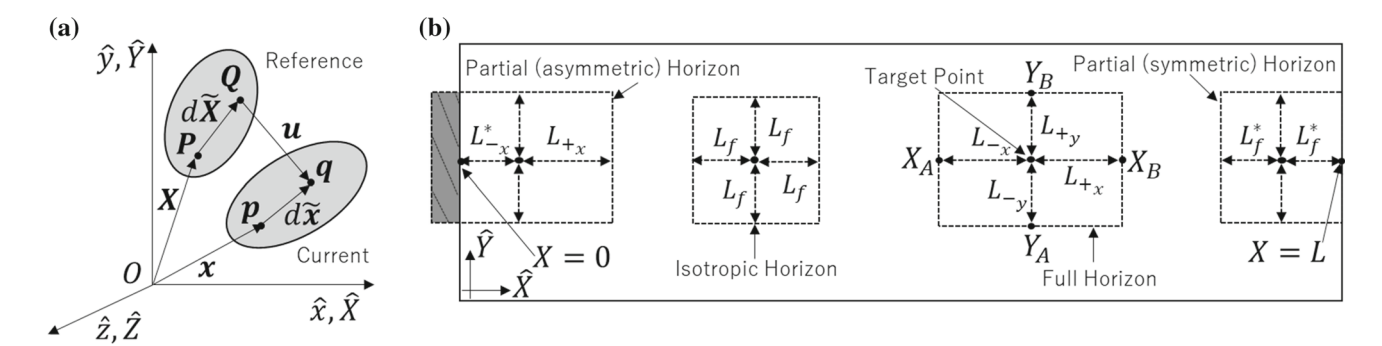


Fig. 1 a Schematic indicating the infinitesimal material and spatial line elements in the nonlocal medium subject to the displacement field \boldsymbol{u} . **b** Horizon of nonlocality and length scales at three different material points in a 2D domain. An isotropic horizon indicates that all the length scales along the different directions are identical to each other. The

truncation of the horizon of nonlocality, that is a partial horizon, can be achieved by either in a symmetric or asymmetric manner as indicated in the figure. For the asymmetric case, that is at X=0, we have $L_{-x}^* < L_{-x} \neq L_{+x}$, while for the symmetric horizon at X=L, we have $L_{-x}=L_{+x}=L_f^*$

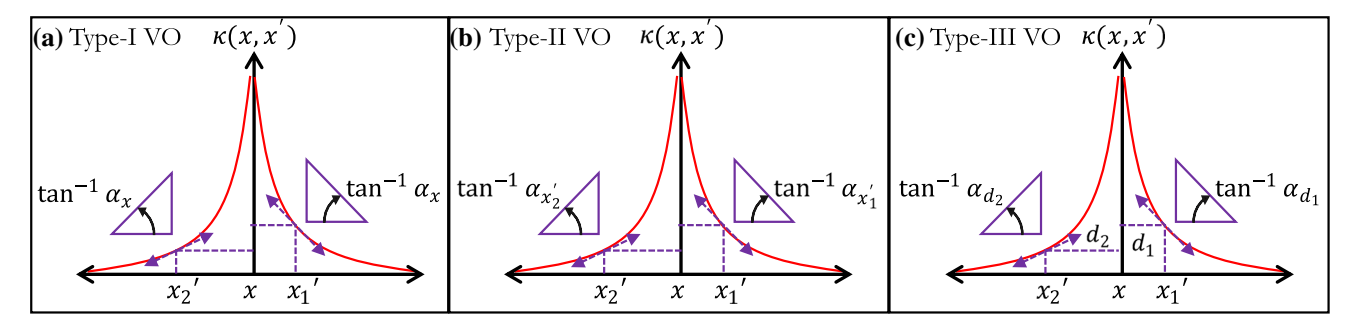


Fig. 2 Schematic illustration of the effect of the functional form of the VO on the strength of the nonlocal interaction between a fixed point x and points in its horizon of nonlocality. The slope indicated at various points corresponds to a logarithmic plot of the kernel of the VO

fractional derivative: $\kappa(x, x') = 1/|x - x'|^{\alpha(x, x')}$. The subscripts used for the different orders indicate the point of evaluation of the VO, for example, $\alpha_{x_1'}$ indicates that the VO is evaluated at x_1'

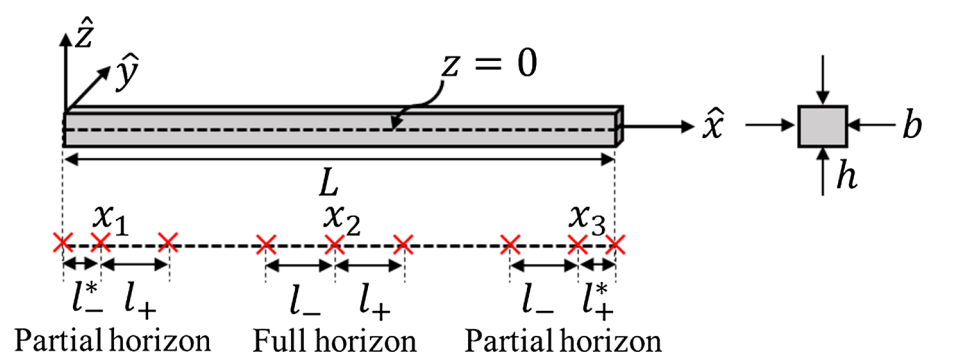
the memory retentiveness of the order history by the VO operator and is different from operator-memory (also called fading memory) that is a measure of the spatial nonlocality in the system. Detailed discussions on order-memory can be found in [30,51]. In the most general approach, the fractional-order at a specific point x, can be chosen as a function of the point x as well as a distant interacting point x', i.e., $\alpha \triangleq \alpha(x, x')$. More specifically, three different types of VO can be defined: (a) Type-I where $\alpha(x, x') \triangleq \alpha(x)$; (b) Type-II where $\alpha(x, x') \triangleq \alpha(x')$; and (c) Type-III where $\alpha(x, x') \triangleq \alpha(x - x')$. In terms of the order-memory, the type-I operator has no spatial order-memory, the type-II operator has a weak spatial order-memory, and the type-III operator has a strong spatial order-memory [30]. A brief discussion on the differences in the definitions of the VO derivatives for the three different order-memory cases is provided in the Appendix A.

In the context of nonlocal elasticity, for the type-I operator, the degree of nonlocality at x depends solely on x and remains unaffected by the points x' in the horizon of nonlocality. In other terms, the strength of interaction between the

point x and any other point x' depends only on the spatial position of x. Similarly, for the type-II operator, the degree of nonlocality at x depends solely on the interacting point x' and for the type-III operator, the degree of nonlocality depends on the spatial vector d = x - x', connecting the interacting point x' with x. These different cases are illustrated in Fig. 2. The functional variation chosen in this study corresponds to the case where $\alpha(x, x') \triangleq \alpha(x)$ (type-I). This choice is due to the fact that it is not always possible to achieve a frame-invariant formulation when employing type-II and type-III definitions (see Appendix B for details). Further, in those selected cases where a frame-invariant model could be achieved (for either type-II or type-III), multiplying factors other than the length scales $(l_{-i}$ and $l_{+i})$ would likely be required within the definition of the VO-RC derivative in Eq. (2). As shown in Appendix B, these factors would need to be numerically evaluated for every point x in the domain of the solid and for every VO. Further, these factors do not admit the same physical interpretation as the length scales introduced in Eq. (2). Hence, in this study, we have limited



Fig. 3 Schematic of the beam illustrating the different geometric parameters. Note the variable nature of the length scales corresponding to the horizon of nonlocality for different points along the length of the beam. The length scales at points close to the boundary of the beam $(x_1 \text{ and } x_3)$ are truncated such that $l_-^* < l_-$ and $l_+^* < l_+$



the formulation to the use of type-I VO that do not carry spatial order-memory.

Finally, we emphasize that, although we focused only on a spatially variable order, the formulation presented above is very general in nature. The formulation could be directly extended to cases where the order-variation depends also on other internal as well as external variables such as, for example, temperature (T), time (t), material microstructure (c), frequency (ω) , strain and stress, or even their combination, i.e., $\alpha \triangleq \alpha(T, t, c, \omega, \varepsilon, \sigma)$.

3 Variable-order model of nonlocal beams

In this section, we develop the constitutive model for a slender nonlocal beam by using the VO continuum formulation developed above. A schematic of the undeformed beam along with the chosen Cartesian reference frame is illustrated in Fig. 3. The top surface of the beam is identified as z = h/2, while the bottom surface is identified as z = -h/2. The width of the beam is denoted as b. The domain corresponding to the symmetry axis of the mid-plane of the beam (i.e., z = 0) is denoted as Ω , such that $\Omega = [0, L]$ where L is the length of the beam. It follows that the 3D domain of the beam can be specified as the tensor product $\Omega \otimes [-b/2, b/2] \otimes [-h/2, h/2]$. For the chosen coordinate system, the axial and transverse components of the displacement field, denoted by u(x, y, z, t) and w(x, y, z, t) at any spatial location x(x, y, z), are related to the mid-plane displacements of the beam according to the Euler-Bernoulli assumptions:

$$u(x, y, z, t) = u_0(x, t) - zD_x^1 w_0(x, t)$$
(4a)

$$w(x, y, z, t) = w_0(x, t)$$
 (4b)

where u_0 and w_0 are the mid-plane axial and transverse displacements of the beam. $D_x^1(\cdot)$ denotes the first IO derivative with respect to the axial spatial variable x. In the following, for a compact notation, the functional dependence of the displacement fields on the spatial and the temporal variables will be implied unless explicitly expressed to be constant. Based

on the above described displacement field, the axial strain in the beam is evaluated using Eq. (1) as:

$$\varepsilon_{xx} = D_x^{\alpha(x)} u_0 - z D_x^{\alpha(x)} \left[D_x^1 w_0 \right] \tag{5}$$

The axial stress σ_{xx} corresponding to the axial strain ε_{xx} is determined using the linear stress-strain relation given in Eq. (3). Note that, for the displacement field given in Eq. (4), a non-zero transverse shear strain would be obtained on using the definition for the nonlocal strain in Eq. (1). However, for the slender beam the rigidity to transverse shear forces is much higher when compared to the bending rigidity. Hence, the contribution of the transverse shear deformation towards the deformation energy of the beam can be neglected [12,17].

By using the above VO fractional constitutive formulation for the nonlocal beam, the total potential energy, in the absence of body forces, is obtained as:

$$\Pi = \underbrace{\frac{1}{2} \int_{\Omega} \sigma_{xx} \varepsilon_{xx} dV}_{\text{Deformation energy}} - \underbrace{\int_{L} u_0 F_a dx}_{\text{Work done by axial forces}} - \underbrace{\int_{L} w_0 F_t dx}_{\text{Work done by transverse forces}}$$
 (6)

where the first integral corresponds to the deformation energy of the beam and the remaining two integrals correspond to the work done by axial F_a and transverse F_t forces, which are applied externally and on the plane perpendicular to the mid-plane of the beam.

Note that by substituting the stress-strain constitutive relation (given in Eq. (3)) within the deformation energy, the fractional-order approach to nonlocality leads to a quadratic and hence, a positive-definite formulation. This convexity ensures that the governing equations, derived in Sect. 3.1 by minimization of the potential energy, are mathematically well-posed and free from boundary effects [12]. This is a key advantage over classical integral approaches to nonlocal elasticity where it is not always possible to achieve a positive-definite formulation, and where additional constitutive boundary conditions are essential to guarantee the well-posed nature of the governing equations [22,23].



3.1 Governing equations

Using the constitutive model presented above, the governing differential equations and the associated boundary conditions are obtained by minimizing the total potential energy of the nonlocal beam given in Eq. (6). The minimization is performed according to variational principles. The quasi-static elastic response of the nonlocal beam modeled by the VO approach is obtained by solving the following system of VO differential equations:

$$\mathfrak{D}_{x}^{\alpha(x')}N_{xx} + F_{a} = 0 \tag{7a}$$

$$D_x^1 \left[\mathfrak{D}_x^{\alpha(x')} M_{xx} \right] + F_t = 0 \tag{7b}$$

and subject to the boundary conditions:

$$I_x^{1-\alpha(x')}N_{xx} = 0 \text{ or } \delta u_0 = 0$$
 (8a)

$$I_r^{1-\alpha(x')}M_{xx} = 0 \text{ or } \delta D_r^1 w_0 = 0$$
 (8b)

$$\mathfrak{D}_{x}^{\alpha(x')}M_{xx} = 0 \text{ or } \delta w_0 = 0$$
 (8c)

In the above equations, N_{xx} and M_{xx} are the axial and bending stress resultants defined as:

$$\{N_{xx}, M_{xx}\} = \int_{-b/2}^{b/2} \int_{-h/2}^{h/2} \{\sigma_{xx}, z\sigma_{xx}\} dz dy$$
 (9)

The detailed derivation of the above governing equations is provided in Appendix C.

In the Eqs. (7,8), $I_x^{1-\alpha(x')}(\cdot)$ is a VO Riesz fractional integral defined as:

$$I_{x}^{1-\alpha(x')}\phi = \frac{1}{2} \left[\underbrace{\int_{x-l_{+}}^{x} l_{+}^{\alpha(x')-1} \frac{\Gamma(2-\alpha(x'))}{\Gamma(1-\alpha(x'))}}_{\text{VO left-handed fractional integral}} \frac{\phi}{(x-x')^{\alpha(x')}} \frac{dx'}{dx'} + \underbrace{\int_{x}^{x+l_{-}} l_{-}^{\alpha(x')-1} \frac{\Gamma(2-\alpha(x'))}{\Gamma(1-\alpha(x'))}}_{\text{VO right-handed fractional integral}} \frac{\phi}{(x'-x)^{\alpha(x')}} \frac{dx'}{dx'} \right]$$

In the above equation l_- and l_+ denote the length scales on the left- and right-hand side of a point on the beam along the x direction (see Fig. 3). $\mathfrak{D}_x^{\alpha(x')}(\cdot)$ is a Riesz Riemann-Liouville (R-RL) derivative with VO $\alpha(x')$ defined as the first IO derivative of the VO Riesz integral defined above:

$$\mathfrak{D}_{x}^{\alpha(x')}\phi = D_{x}^{1} \left[I_{x}^{1-\alpha(x')}\phi \right] \tag{11}$$

Note that the VO fractional derivative $\mathfrak{D}_{x}^{\alpha(x')}(\cdot)$ and the VO fractional integral $I_{x}^{1-\alpha(x')}(\cdot)$ are defined over the interval $(x-l_{+},x+l_{-})$ unlike the VO-RC derivative $D_{x}^{\alpha(x)}(\cdot)$ which

is defined over the interval $(x - l_-, x + l_+)$. Further, these operators possess weak order-memory (type-II) unlike the VO-RC derivative which possesses no order-memory (see discussion in Sect. 2 or Appendix A). This change in the terminals of the interval and memory characteristic of the R-RL fractional integral and derivative follows from simplifications during the variational process (see Appendix C). In fact, this process shows that the adjoint operator for the VO-RC fractional derivative, present in the definition of the VO strain, is the VO R-RL fractional derivative defined in Eq. (11).

The VO beam governing equations and boundary conditions given in Eqs. (7, 8) can be expressed in terms of the displacement field variables by using the constitutive stress-strain relations of the beam. Here below, we provide the governing differential equations in terms of the displacement field variables for an isotropic beam:

$$E_0 b h \mathfrak{D}_x^{\alpha(x')} \left[D_x^{\alpha(x)} u_0 \right] + F_a = 0$$
 (12a)

$$-\frac{1}{12}E_0bh^3D_x^1\left[\mathfrak{D}_x^{\alpha(x')}\left[D_x^{\alpha(x)}\left(D_x^1w_0\right)\right]\right] + F_t = 0 \quad (12b)$$

where E_0 denotes the modulus of elasticity of the isotropic beam. The corresponding boundary conditions are obtained as:

$$E_0 bh I_x^{1-\alpha(x')} \left[D_x^{\alpha(x)} u_0 \right] = 0 \text{ or } \delta u_0 = 0$$
 (13a)

$$E_0 b h^3 I_x^{1-\alpha(x')} \left[D_x^{\alpha(x)} \left(D_x^1 w_0 \right) \right] = 0 \text{ or } \delta D_x^1 w_0 = 0$$
(13b)

$$E_0bh^3\mathfrak{D}_x^{\alpha(x')}\left[D_x^{\alpha(x)}\left(D_x^1w_0\right)\right] = 0 \text{ or } \delta w_0 = 0 \qquad (13c)$$

Note that the governing equations for the axial and transverse displacements are uncoupled, similar to what is seen in the classical (local) Euler-Bernoulli beam formulation. Further, as expected, the classical Euler-Bernoulli beam governing equations and boundary conditions are recovered for $\alpha=1$ throughout the domain.

Assuming that the deformation process of the nonlocal beam is continuous and invertible, it follows that the displacement field u(x) belongs to a class ψ of all kinematically admissible displacement fields such that every $u(x) \in \psi$ is continuous and differentiable everywhere within the solid, apart from satisfying the displacement boundary conditions. With this condition on the admissible displacement fields we prove the following:

Theorem 1 The set of linear operators describing the governing VO differential Eqs. (12, 13) of the beam are self-adjoint.



Proof First, we present the proof for the self-adjointness of the VO differential operator of the governing equation representing axial motion of the isotropic beam:

$$\tilde{\mathbb{L}}(\cdot) = \mathfrak{D}_{x}^{\alpha(x')} \left[D_{x}^{\alpha(x)}(\cdot) \right] \tag{14}$$

Note that the fractional operator $\tilde{\mathbb{L}}(\cdot)$ is linear in nature [30]. We consider the inner-product $\langle \tilde{\mathbb{L}}(u_0), v_0 \rangle$ such that u_0 and v_0 satisfy the boundary conditions given in Eq. (13):

$$\langle \tilde{\mathbb{L}}(u_0), v_0 \rangle = \int_0^L v_0 \, \mathfrak{D}_x^{\alpha(x')} \left[D_x^{\alpha(x)} u_0 \right] \mathrm{d}x \tag{15}$$

Using the definition of the VO R-RL derivative given in Eq. (11) the above integration is expressed as:

$$\langle \tilde{\mathbb{L}}(u_0), v_0 \rangle = \int_0^L v_0 \frac{\mathrm{d}}{\mathrm{d}x} \left[\int_{x-l_+}^x \frac{1}{2} l_+^{\alpha(x')-1} \frac{\Gamma(2-\alpha(x'))}{\Gamma(1-\alpha(x'))} \frac{D_{x'}^{\alpha(x')} u_0}{(x-x')\alpha(x')} \mathrm{d}x' \right] \mathrm{d}x + \int_0^L v_0 \frac{\mathrm{d}}{\mathrm{d}x} \left[\int_x^{x+l_-} \frac{1}{2} l_-^{\alpha(x')-1} \frac{\Gamma(2-\alpha(x'))}{\Gamma(1-\alpha(x'))} \frac{D_{x'}^{\alpha(x')} u_0}{(x'-x)^{\alpha(x')}} \mathrm{d}x' \right] \mathrm{d}x$$

$$(16)$$

We further evaluate the above integrals using integration by parts to obtain the following:

$$\langle \tilde{\mathbb{L}}(u_{0}), v_{0} \rangle = v_{0} I_{x}^{1-\alpha(x')} \left[D_{x}^{\alpha(x)} u_{0} \right]_{0}^{L}$$

$$- \int_{0}^{L} \frac{dv_{0}}{dx} \left[\int_{x-l_{+}}^{x} \frac{1}{2} l_{+}^{\alpha(x')-1} \frac{\Gamma(2-\alpha(x'))}{\Gamma(1-\alpha(x'))} \frac{D_{x'}^{\alpha(x')} u_{0}}{(x-x')^{\alpha(x')}} dx' + \int_{x}^{x+l_{-}} \frac{1}{2} l_{-}^{\alpha(x')-1} \frac{\Gamma(2-\alpha(x'))}{\Gamma(1-\alpha(x'))} \frac{D_{x'}^{\alpha(x')} u_{0}}{(x'-x)^{\alpha(x')}} dx' \right] dx$$

$$(17)$$

We exchange the order of integration in the above integrals and further, use the boundary conditions in Eq. (13) to obtain the following expression:

$$\langle \tilde{\mathbb{L}}(u_0), v_0 \rangle = \int_0^L \frac{1}{2} \frac{\Gamma(2 - \alpha(x'))}{\Gamma(1 - \alpha(x'))} D_{x'}^{\alpha(x')} u_0$$

$$\left[l_+^{\alpha(x') - 1} \int_{x'}^{x' + l_+} \frac{D_x^1 v_0}{(x - x')^{\alpha(x')}} dx \right]$$

$$+ l_-^{\alpha(x') - 1} \int_{x' - l_-}^{x'} \frac{D_x^1 v_0}{(x' - x)^{\alpha(x')}} dx$$
(18)

Using the definition of the VO-RC derivative given in Eq. (2), the above integral is simplified as:

$$\langle \tilde{\mathbb{L}}(u_0), v_0 \rangle = \int_0^L D_{x'}^{\alpha(x')} u_0 \ D_{x'}^{\alpha(x')} v_0 \ dx'$$

$$\equiv \int_0^L D_x^{\alpha(x)} u_0 \ D_x^{\alpha(x)} v_0 \ dx$$
(19)

By exploiting the symmetry in the above expression, we can write the following:

$$\langle u_0, \tilde{\mathbb{L}}(v_0) \rangle = \int_0^L D_x^{\alpha(x)} u_0 \ D_x^{\alpha(x)} v_0 \ dx$$
 (20)

Comparing Eq. (19) and Eq. (20), the VO differential operator $\tilde{\mathbb{L}}(\cdot)$ is evidently self-adjoint. By retracing the steps outlined above, it can be similarly shown that the operator describing the transverse governing equation of the beam is also self-adjoint in nature. For the sake of brevity, we skip the proof here. This demonstration establishes the claim in Theorem 1.

Recall that the quadratic nature of the deformation energy density was used to emphasize that the system is positivedefinite in nature. The same claim is also established from the self-adjoint nature of the governing equations presented in Eqs. (19, 20). This can be easily verified by considering $\langle \tilde{\mathbb{L}}(u_0), u_0 \rangle$ in the Eq. (19), which results in a quadratic form within the integral. Note that the self-adjointness and positive-definiteness of the system hold independently of the boundary conditions. This is a particularly remarkable result because, as established in the literature, it is not always possible to define a self-adjoint quadratic potential energy for the classical integral approach to nonlocal elasticity [22,23]. As discussed previously, this characteristic leads to well-posed governing equations and consistent predictions regardless of the boundary conditions [12,24] as well as it enables the formulation of finite element based approaches for the numerical simulation of the complex nonlocal governing equations.

Theorem 2 The displacement field u(x) which solves the set of governing equations and boundary conditions in Eqs. (7–8) (if it exists) is unique in the class ψ . Further, the strain and stress fields $\varepsilon(x)$ and $\sigma(x)$ corresponding to the solution u(x) are also unique.

Proof The proof of the above theorem follows exactly the proof provided for the CO formulation [12] and it is not repeated here for the sake of brevity.

4 Fractional model parameter estimation: methodology

A critical issue in the use of fractional-order models is the determination of the order parameter, either in its constant or variable form. The strategy to determine the order can vary depending on the underlying source of the fractional behavior. In other terms, we could classify the use of fractional-order models based on their main application or, equivalently, on the reason that induces the fractional nature of the system. From a high level perspective, fractional models can be employed to: (P1) simplify models while

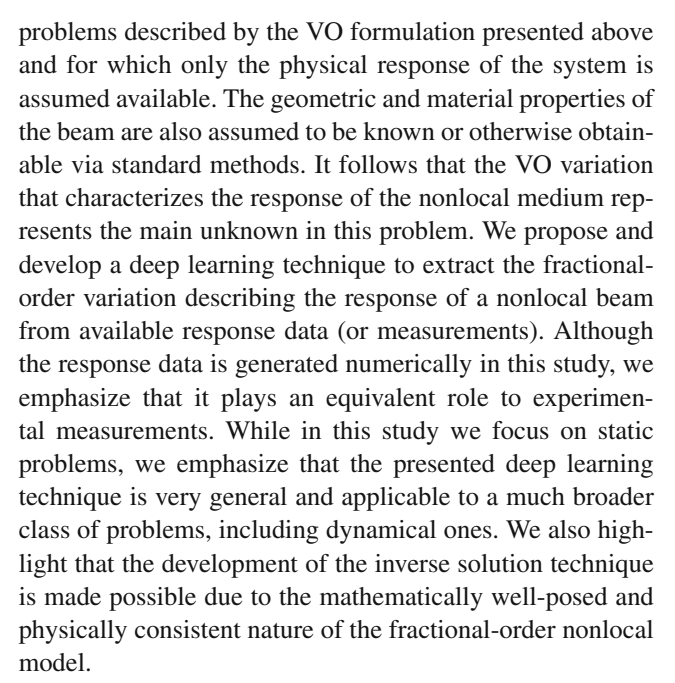


maintaining accuracy (e.g. fractional homogenization and model-order reduction), (P2) model complex nonlinear and evolutionary behavior (e.g. contacts, dislocations, dynamic fracture), and (P3) to capture physical mechanisms that are intrinsically fractional and, as such, not fully described by IO operators (e.g. anomalous and hybrid transport processes). Depending on the particular class the problem at hand belongs to, the strategy to determine the appropriate order can vary significantly.

In the first class of problems (P1), wherein fractional calculus is applied with the intent of simplifying the model, the fractional-order could be determined by a direct matching technique based on selected properties of the solids such as, for example, attenuation and dispersion behavior [1,2,10,20]or scattering fields [8,9]. In the case of evolutionary nonlinear problems (P2), such as contact dynamics, viscoelastic mechanics, motion of dislocations in lattice structures, and dynamic fracture, physics-driven laws could be defined and embedded in the VO definition so to determine the order variation based on the instantaneous response of the system. Examples include physical laws to detect transitions across different physical states such as the status of a contact [32,33], the formation and annihilation of pairwise interparticle bonds [38], the state of damage [39], and the order of viscoelastic damping [31,32].

While the order characterizing the first two classes of applications (P1 and P2) can be obtained via well established analytical (deterministic) methods described above, there is no specific strategy to obtain the fractional-order for the third class of applications (P3). Although, in this latter class, the occurrence of the fractional behavior can be connected to certain underlying physical mechanisms (e.g. nonlocal behavior associated with porous media, multiple scattering in periodic or disordered media), in general there is no unique approach to identify the order. These problems often resort to data fitting selected characteristics of fractional models against experimentally obtained data using standard regression techniques [5–7,26,27,40,50,52]. As an example, consider the static response of a porous solid with unknown porosity. In this scenario, it is not possible to obtain an analytical expression of the fractional-order describing the static response of the solid. The elliptic nature of the problem and the intricate geometry further complicate this task. More generally speaking, it is typically not possible to obtain analytical closed-form expressions for key physical quantities (such as, for example, the potential energy) that would provide the foundation for an analytical order determination technique similar to P1 and P2. Hence, in this class of problems, a strategy to determine the fractional-order characteristics based on the measured experimental response of the system becomes an indispensable tool.

In this study, we focus on problems belonging to the third class. In particular, we consider nonlocal elasticity



In the following, we first formulate the inverse problem which consists in identifying the VO $\alpha(x)$ describing a nonlocal beam, from available response data. Then, we present the architecture of the neural network used to solve the inverse problem, and we discuss dataset generation, network training, and numerical predictions.

4.1 Problem definition

Consider a benchmark problem consisting in a nonlocal beam clamped at both its ends and subject to a uniformly distributed transverse load (UDTL) of magnitude 1N/m. Given the transverse displacement w_0 and rotation θ_0 of the midplane of the beam, the objective is to characterize the VO $\alpha(x)$ using a deep bidirectional recurrent neural network (BRNN). Recall that, for an Euler-Bernoulli, the rotation is approximated as the first IO derivative of the beam deflection, that is, $\theta_0 = D_r^1 w_0$. Note that we focus only on the transverse response of the beam. The methodology outlined in the following extends directly to an inverse problem involving either axial or both axial and transverse deformations. Without the loss of generality, we assumed that the beam is isotropic and has a uniform cross section along its length. The material properties and dimensions of the beam used in this study are provided in Table 1. Further, the horizon of nonlocality was assumed to be isotropic such that the length scales l_{-} and l_{+} are equal to a constant l_{f} for points sufficiently within the domain of the beam. These length scales are truncated for points close to the beam boundaries as discussed in Sect. 2 (see Fig. 3). Note that the length scales can also be determined by using the network architecture presented below. In this regard, note that the length scale is typically known a priori from geometric considerations such



Table 1 Beam dimensions and material properties

Property	E ₀ (MPa)	ν	L(m)	h (m)	b (m)	l_f (m)
Value	30	0.3	1.0	0.02	0.02	0.2

as presence of specific geometric features and intentionally designed long range connections [53], and in fact, is fixed to be the entire length of the solid in a majority of the approaches (classical as well as fractional) [20,53,54].

Before proceeding further, we make some remarks on the macroscale nature of the chosen problem. First we emphasize that the formulation presented in this study is highly general and applicable irrespective of the specific spatial scale and material properties. Further, note that nonlocal effects are observed in different classes of materials irrespective of the spatial scale. A detailed investigation of literature suggests the role of nonlocal effects have been primarily investigated in nano- and micro-structures, and applications to macrostructures are limited. This is not surprising since nonlocal effects, that are typically attributed to long-range forces, are prominent in nano- and micro-structures as Van der Waals, surface forces or nonlocal atomic interactions [54– 56]. The contribution of these interactions are insignificant in macrostructures where nonlocal effects typically originate from material heterogeneities [10,20] (as we will demonstrate in Sect. 6) and even intentionally nonlocal designs [53,57]. While interactions between dissimilar material cells (e.g. periodic media) or layers (e.g. functionally graded materials) occur naturally in heterogeneous materials [10,20], these are induced artificially via specially designed short and/or long range connectors in the intentional nonlocal designs [53,57].

4.2 Network architecture

This section describes the network architecture used to predict the fractional-model parameters. The network architecture used to extract the VO $\alpha(x)$ contains a combination of fully connected layers and a bidirectional recurrent neural network (BRNN), as illustrated in Fig. 4 [41].

In order to determine the appropriate structure of the network to solve the inverse problem, we started from two popular types of neural network, 1D convolutional neural networks [45] and convolutional long short term memory deep neural network (CLDNN) [58]. We selected the convolutional network since it can locally extract and combine features from its input in order to predict the output. However, results showed that the convolutional network could not accurately solve the inverse problem, even when using a large number of trainable parameters. In an effort to increase the performance of the network, we employed a CLDNN which includes recurrent long-short term memory layers capable of

learning memory effects in a system. While recurrent neural networks have proven to be highly accurate in several classes of problems [44], witnessing poor prediction performance of CLDDN motivated us to use BRNN, which is an extension of recurrent neural network, to solve the inverse problem. The choice of BRNN in the development of the network architecture is further justified by the finite nature of the quasi-static nonlocal problem. Recall that recurrent cells have the capacity to learn the recursive logic relating a sequential parameter to a sequential input and are effective for time-dependent signals. The recurrent cells process the input sequence in a preferential direction starting from the first member of the sequence (forward) and hence, do not consider the effect of the cells in the reverse direction on the current output. This characteristic is perfectly suitable for physical systems characterized by a preferential direction of propagation of information. However, for finite systems (either local or nonlocal), the response at a point is influenced by the boundary conditions. Additionally, for nonlocal systems, the response of a point is influenced also by the response of a collection of points within a fixed length scale. Hence, a unidirectional (either forward or backward) flow of information is expected to cause insensitivity of the predictions, hence reducing the network accuracy. This limitation is overcome by BRNN, where two sets of recurrent cells process the input data sequence in two opposite directions: (1) forward that processes the input starting from its first member, and (2) backward that starts from the last member of the sequence. The output of the recurrent cells in each direction is then combined in either a linear or nonlinear fashion to calculate the output corresponding to each member of the input sequence. A detailed description of the recurrent and bidirectional neural networks can be found in [41,45]. In addition to the BRNN layer, we also used fully connected layers to increase the the number of trainable parameters of the network and to enhance the learning capacity of the network.

A schematic of the network used in this study is provided in Fig. 4. The input to the network consists of a sequence of nodal beam deflections and rotations. This input is obtained by simulating the response of the beam to a UDTL via the fractional-order finite element method (f-FEM) [12] (performed via an in-house finite element model code) or it could be an experimentally acquired response. The f-FEM builds on the algorithm proposed in [12], that was initially developed for CO fractional differential equations describing the response of nonlocal beams with a fixed strength (CO) of nonlocality. However, the same numerical algorithm extends to the VO model directly, with the only provision that the CO is replaced by the point-wise (spatially) varying value of the VO. More specifically, the CO used in the numerical integration of the stiffness matrix of the nonlocal beam at the Gauss quadrature points, is replaced by the local value of the VO at the same point. The remaining formulation remain



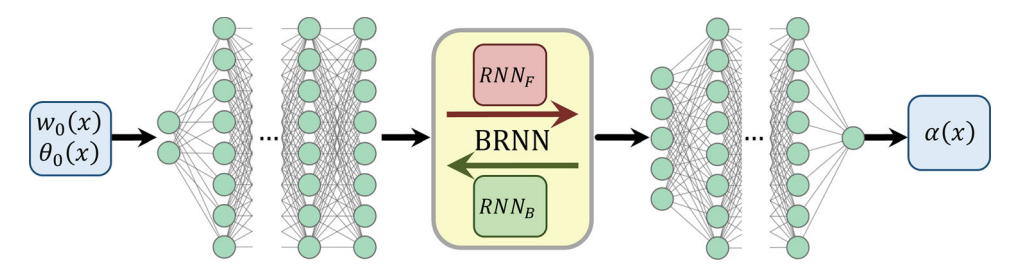


Fig. 4 Schematic of the network architecture used to identify the VO $\alpha(x)$. The network consists of both fully connected layers and a bidirectional recurrent neural network (BRNN). The BRNN includes two sets

of recurrent networks to process the input sequence in both the forward (RNN_F) and the backward (RNN_B) directions. Given the sequence of nodal w_0 and θ_0 the network predicts α at each node

Table 2 Specific details of the different layers within the network architecture. The network input is a sequence of the nodal displacement w_0 and rotations θ_0 having a cumulative size of [201×2]. The output is an array of nodal fractional-order $\alpha(x)$ of size [201×1]

Layer #	Layer type	Size	Layer #	Layer type	Size
1	fully connected	100	6	fully connected	50
2	fully connected	100	7	fully connected	100
3	fully connected	100	8	fully connected	100
4	fully connected	100	9	fully connected	100
5	bidirectional	100	10	fully connected	100

unchanged, and hence, for the sake of brevity, we do not provide the details of the finite element formulation. The interested reader is referred to [12] for the complete mathematical treatment.

For each sample problem, 200 uniform elements (corresponding to N = 201 equally spaced nodes) were used to discretize the beam and to numerically calculate its deformation field. Hence, the size of the network input sequences is [201 \times 2] consisting of the nodal transverse displacement w_0 and rotation θ_0 . The input is passed to 5 fully connected layers with 100 neurons in each layer and a hyperbolic tangent activation function. The input layer is followed by a bidirectional layer, with 100 long-short-term-memory (LSTM) units [59] in both the forward and backward directions. The output of the bidirectional layer is then passed to 5 fully connected layers with a rectified linear unit (ReLU) activation function connected to the output layer [45]. The network output layer has one node and a linear activation function. The output layer returns a sequence of the VO $\alpha(x)$ whose members correspond to the input sequence members; in other terms, the nodal values of the VO. Table 2 summarizes the above mentioned details of the network architecture. The number of nodes in different layers of the network architecture was obtained via a trial and error procedure while monitoring the accuracy of the prediction.

4.3 Dataset generation and network training

To generate the training dataset, sample distributions of $\alpha(x)$ were defined and the corresponding responses of the beam were obtained via the f-FEM. For each case (i.e. for each VO distribution), the beam was subjected to a UDTL. For each simulation, the transverse displacement w_0 , rotation θ_0 , and the fractional-order α of all the nodes were recorded. The VO of the sample problems was chosen to be either random or a predefined function. In the case of random VO, the value of the fractional-order at each nodal location along the length was chosen randomly from a uniform distribution within the range [0.7, 1]. Additionally, three different functions were used to generate deterministic distribution of VO: (1) linear, (2) sinusoidal, and (3) polynomial. These functions were defined as:

Linear:
$$\alpha_l(x) = (a_1 - a_0)x + a_0 \ 0.7 \le a_0, \ a_1 \le 1.0$$

Sinusoidal: $\alpha_s(x) = b_0 + 0.1 \left| \sin \left(\frac{b_1 x}{L} \right) \right|$
 $+ \cos \left(\frac{b_2 x}{L} \right) \left| \ 0.7 \le b_0 \le 0.8,$
 $0 \le b_1, b_2 \le 1.0$
Polynomial: $\alpha_p(x) = c_{10} x^{10} + c_9 x^9 + ...$

Polynomial: $\alpha_p(x) = c_{10}x^{10} + c_9x^9 + \dots + c_1x + c_0 \, 0.7 \le \alpha_3(x) \le 1.0$ (21)



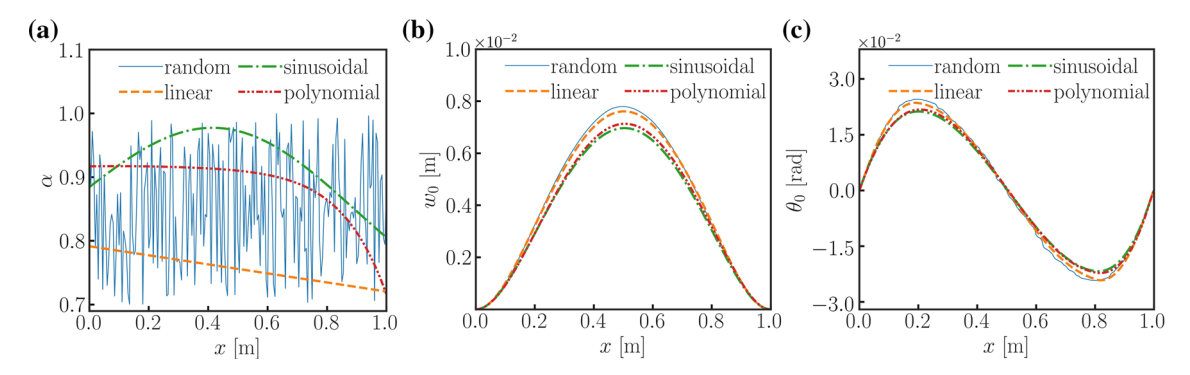


Fig. 5 Samples of the four fractional-order types in the generated dataset and their corresponding beam response: **a** variable fractional-order $\alpha(x)$, **b** rotation $\theta_0(x)$, and **c** deflection $w_0(x)$

The random distribution, along with the above definitions for the VO law, ensure that the network is exposed to different patterns of $\alpha(x)$ during the training procedure. This approach allows the trained network to solve problems with a variety of $\alpha(x)$ distributions, including those never seen by the network during the training process. More specifically, in Sect. 5 we have shown that the trained network accurately predicts the $\alpha(x)$ distributions consisting of Bessel functions and hyperbolic tangent functions that did not belong to the training dataset. In each case, the variation was chosen such that $0.7 \le \alpha(x) \le 1$. While the structure of the network is insensitive to the specific range of $\alpha(x)$ and could be applied to any arbitrary interval, the selected VO range was chosen to avoid physical instabilities that are known to occur for very small values of the fractional-order [12,24] (i.e. for extreme level of nonlocality). Samples of $\alpha(x)$ distribution along the beam length are provided in Fig. 5a. For each distribution of $\alpha(x)$, 4×10^4 samples were generated and solved. Hence, the dataset contains 1.6×10^5 samples. Out of the total sample cases, 85% were used for training and the remaining 15% were used for validation.

The network is trained using a mean square error loss function defined as:

$$\mathcal{L}\left[\mathcal{N}(w_0, \theta_0; \mathbb{W})\right] = \frac{1}{N_b} \sum_{i=1}^{N_b} |\mathcal{N}(w_0, \theta_0; \mathbb{W}) - \boldsymbol{\alpha}_{true}|^2$$
(22)

where \mathcal{N} is the network, \mathbb{W} is a vector that includes all the network's trainable parameters (network layers weights and biases), N_b is the batch size, and α_{true} is the vector containing true values of nodal α corresponding to the network input w_0 and θ_0 obtained from the training dataset. The optimal order prediction is obtained by minimizing the loss for network parameters \mathbb{W}^* as follows:

$$\mathbb{W}^* = \arg\min_{\mathbb{W}} \ \mathcal{L}[\mathcal{N}(w_0, \theta_0; \mathbb{W})]$$
 (23)

The network was built using Python Keras and Tensorflow packages. We used Xavier initialization method [60] for the layers weights and zero initialization for the biases. We trained the network using the Adam [61] algorithm for 7000 epochs with a batch size of 2048 and the loss function defined in Eq. 22. The initial learning rate (LR) was set to .001 and we used a LR scheduler that divides the LR by a factor of 2 every 3000 epochs. The dataset and network training hyper parameters are summarized in Table 3.

From Fig. 5, we observe that the trend of the static response of the beam (particularly the transverse displacement) does not drastically change for the different VO $\alpha(x)$ laws. We emphasize that this behavior is a direct outcome of the nature of the loading (UDTL) and of the prescribed boundary conditions (clamped at both ends). In fact, nonlocal beams with a CO (that is, $\alpha(x) = \alpha_0$) generate a maximum displacement at the mid-point when subject to a UDTL under the prescribed boundary condition. The deformed shape of the beam remains unchanged irrespective of the specific value of α_0 . Increasing the degree of nonlocality by decreasing α_0 determines a softening of the beam, which merely increases the maximum transverse displacement [12,17]. Consequently, the only major effect of the VO $\alpha(x)$ consists in shifting the location on the beam where the maximum transverse displacement occurs. More specifically, for VO laws that are asymmetric about the mid-point of the beam, the maximum transverse displacement no longer occurs at the mid-point of the beam. This aspect is more evident from the results demonstrating the response of different heterogeneous beams in Sect. 6.

5 Variable-order identification: numerical results

In this section, we present and discuss the application of the trained network to solve the inverse problem consisting in determining the spatial variation of fractional-order in a



Table 3 Training dataset and network training hyper-parameters. Learning rate scheduler step refers to the number of epochs after which the LR scheduler divides the learning rate by the division factor

Parameter	Training dataset size	Validation dataset size	Training epoch	Initial learning rate	LR scheduler step	LR scheduler division factor
Value	1.36×10^{5}	2.4×10^{4}	7000	0.001	3000	2

nonlocal beam given its response to an externally applied load. We consider seven sample test cases to show the efficacy of the inverse approach. The difference between these sample cases consists in the functional distribution of the VO $\alpha(x)$ along the beam length. Test cases 1 to 4 are randomly selected from the test dataset and have (1) random, (2) linear, (3) sinusoidal, and (4) polynomial VO, respectively. For cases 5 and 6, the VO $\alpha(x)$ was defined using Bessel and hyperbolic tangent functions, respectively. The test case 7 contains a problem with CO α . The objective in the first four cases is to demonstrate that the network can accurately identify the VO $\alpha(x)$ in problems that have the same type of VO $\alpha(x)$ as the samples in the training dataset. Cases 5, 6, and 7 are defined and solved to further evaluate the performance of the network in situations where the VO $\alpha(x)$ patterns were never seen by the network during the training phase. This class of data are referred to be inconsistent with the training dataset. Further, we also analyzed the performance of the network in the presence of noisy input, for the test cases 1 to 4. Each sample case, irrespective of the presence or absence of noise, considers the response of the beam with the properties and loading conditions defined in Sect. 4.1. In the following, we first present the network training results and then discuss the network predictions for the different sample cases.

Before proceeding further, we make a few remarks on the selection of the number of measurement points used to determine the VO $\alpha(x)$. First, the number of measurement points needed for a given scenario depends on the rate of change of the VO $\alpha(x)$ or, in a more general case, on the rate of change of both the length scale (l_f) and the VO $\alpha(x)$. From a general perspective, the measurement points should be dense enough to avoid any spatial aliasing of the measured displacement field. The importance of having a sufficient number of measurements can be better seen from the random $\alpha(x)$ case (see Fig. 5a and Fig. 7a). In this case, the sharp spatial rate of change in the VO α , results in a non-smooth profile of the rotation degree of freedom (see Fig. 5c and Fig. 8a). In such cases, a drastic reduction in the number of measurement points tends to alias the displacement field (the network input) and renders the inverse problem (leading to the distribution of $\alpha(x)$ ill-conditioned. On the other hand, the number of measurement points can be reduced following any a priori knowledge on a low spatial rate of change in VO $\alpha(x)$ (such as the cases shown in Fig. 7b–d), and the network can still be trained to accurately predict the VO $\alpha(x)$ from

the corresponding measurements. In the above discussion, we have implicitly assumed that the number of measurement points is equal to the number of data points used to sample the VO $\alpha(x)$.

Finally, when the number of measurement points is greater than the data points used to sample the VO $\alpha(x)$, appropriate interpolation techniques must be used to predict the $\alpha(x)$. In fact, we used cubic spline interpolation in this study in the modeling of porous beams (Sect. 6) to predict $\alpha(x)$ for regions where some pores overlap with the symmetry axis of the beam. These regions can be directly identified from the 3D finite element simulations presented in Figs. 15c–19c. As evident from the results presented in Figs. 15c–19c, this interpolation does not affect the predicted VO response in the remaining parts of the porous beam, and the overall accuracy of the approach is excellent (which we will discuss in detail in Sect. 6). In this regard, we emphasize that the efficiency of the interpolation of $\alpha(x)$ is directly related to the ability of the chosen set of interpolation points (or measurement points) in capturing the response at different scales within the structure. In other terms, the set of measurement and interpolation points must be chosen such that they capture the deformed shape properly, without aliasing the response. As an example, the set of points chosen in the case of porous beams were able to capture the rotation, which as evident from Fig. 15c-19c is localized on a shorter scale (in comparison to the size of the beam) due to the random distribution of pores. Thus, when the variation of the response (not necessarily the underlying geometric or material features) occurs on certain characteristic scales, the interpolation and grid points should be fine enough not to alias the response at these scales. We note that these considerations on the spatial discretization are standard practice in most structural simulations or experiments and are not related or influenced by the specific features of the VO formulation.

5.1 Network training

The network is trained using the hyper-parameters presented in Sect. 4.3. Figure 6 shows the trend of the loss function versus the epoch number during the network training. It is seen that the loss function for both the training and validation data sets converge to similar values, indicating that the trained network is not over-fitted on the training dataset. The mean relative prediction percentage error of the trained network



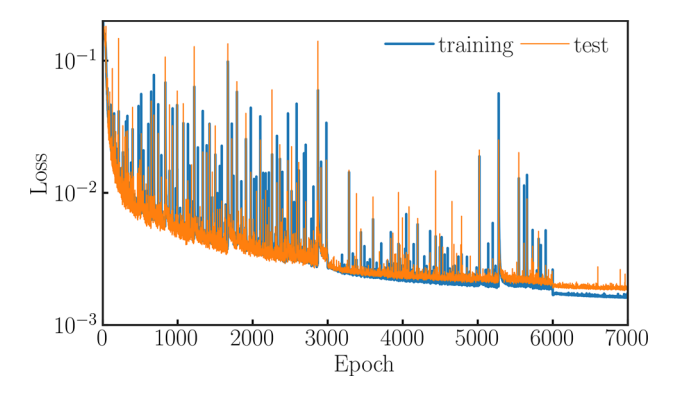


Fig. 6 Loss function versus the epoch number for the training and test data sets. Loss function value at the last epoch is 0.00160 for the training dataset and 0.00191 for the test dataset

over the test dataset is 0.26%. The error corresponding to a given dataset is defined as:

$$Er = \frac{1}{N} \sum_{i=1}^{N} \left| \frac{\alpha_{net}(x_i) - \alpha_{true}(x_i)}{\alpha_{true}(x_i)} \right| \times 100$$
 (24)

where N denotes the number of nodes in the f-FEM mesh used to simulate the VO beam, x_i denotes the nodal coordinate, α_{true} is the actual value of the fractional-order and α_{net} is the network prediction. $|(\cdot)|$ denotes that absolute values of the nodal error (that is, the L_1 norm) are used to calculate the mean error. An important aspect to highlight is that, although there is a small difference between the response of the beam for different distributions of $\alpha(x)$, as evident from the sample problems presented in Fig. 5, the network successfully distinguishes between the different closely-valued beam responses and accurately predicts the $\alpha(x)$.

5.2 Identification of the fractional-order based on consistent VO distributions

We discuss the performance of the network in terms of identification of the VO $\alpha(x)$ consistent with the training dataset, containing the test cases 1 to 4. The network predictions for the test cases 1-4 are compared with the actual value of the VO $\alpha(x)$ in Fig. 7. The mean nodal percentage prediction error is obtained as 0.85%, 0.03%, 0.12%, and 0.06% for the cases 1–4, respectively. The extremely low prediction errors prove that the trained network can accurately identify the variable fractional-order irrespective of its functional type, given the beam deformation. Using the predicted VO $\alpha(x)$, the response of the beam was re-calculated via the f-FEM and compared with the beam deformation obtained using the exact VO, in Fig. 8. As expected, the accurate predictions of the VO $\alpha(x)$ lead to an excellent match between the two deformation results.

5.3 Identification of the fractional-order based on inconsistent VO distributions

In order to establish the efficacy of the architecture in predicting the VO, we tested the performance of the network for different order variations that were not available to the network during training (that is, for order variations inconsistent with the training dataset). The order variations for the cases 5 to 7 are assumed as:

Bessel: $\alpha_5(x) = 0.428 \, \mathbf{J}_5(10x) + 0.820$

Hyperbolic tangent: $\alpha_6(x) = 0.102 \tanh(6x - 2) + 0.848$

Constant: $\alpha_7(x) = 0.9$

(25)

where $J_5(\cdot)$ denotes the fifth-order Bessel function of the first kind. Figure 9 compares the network predictions and the actual distributions of the VO $\alpha(x)$. The mean relative prediction percentage error for the cases 5–7 were 0.22%, 0.50%, and 0.03%, respectively. The accurate predictions demonstrate that the network is highly capable of identifying the VO $\alpha(x)$ corresponding to problems with VO $\alpha(x)$ distributions unseen by the network in the training process. This is critical for the successful application of the network to real-world problems (similar to those considered in Sect. 6), where the VO describing the system response are inconsistent with the order variations assumed in the training dataset.

5.4 Identification of the fractional-order from noisy data

In this section, we assessed the performance of the network in the presence of noisy input data, corresponding to the test cases 1–4 in Sect. 5.2. For this purpose, we added numerically generated noise to the nodal values of w_0 and θ_0 . We assumed the noise has a Gaussian distribution with the following probability density function:

$$\tilde{p}(z) = c_0 e^{-\frac{(z-\mu_0)^2}{2s_0^2}} \tag{26}$$

where $\mu_0 = 0$ is the mean value, s_0 is the standard deviation, and c_0 is a scaling factor. s_0 is expressed as:

$$s_{w_0} = c_0 \tilde{s}_{w_0}$$

$$s_{\theta_0} = c_0 \tilde{s}_{\theta_0}$$
(27)

where s_{w_0} and s_{θ_0} are the standard deviations of the noise added to w_0 and θ_0 degrees of freedom, respectively (see Eq. 26). \tilde{s}_{\square} is the standard deviation of w_0 or θ_0 calculated over absolute values of all the samples in the training dataset. We assessed the performance of the network for three different values of c_0 , $c_0 = \{0.25, 0.5, 0.75\}$. For each case, we



Fig. 7 VO $\alpha(x)$ distributions predicted by the network α_{net} , compared with their corresponding actual values α_{true} for four different distribution types: a Case 1: randomly varying $\alpha(x)$, **b** Case 2: linear $\alpha(x)$, c Case 3: sinusoidal $\alpha(x)$, and **d** Case 4: polynomial $\alpha(x)$. As evident, the spatial variation of the VO $\alpha(x)$ is predicted very accurately by the network

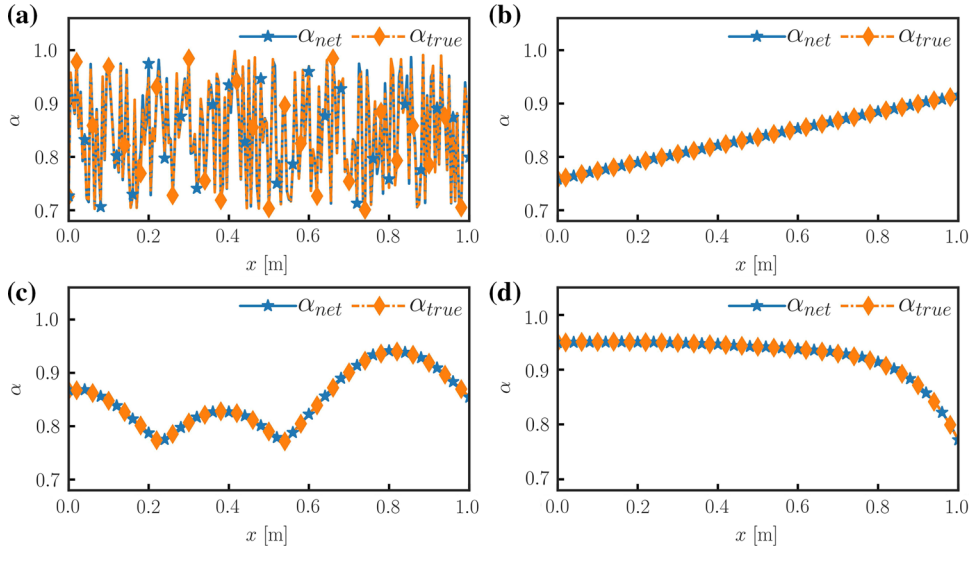


Fig. 8 Comparison of the actual beam displacement $w_{0_{true}}$ and beam rotation $\theta_{0_{true}}$ with the response calculated by using the VO α_{net} distribution predicted by the network within the f-FEM. Four different variations of $\alpha(x)$ are considered: **a** random, b linear, c sinusoidal, and d polynomial

0.2

0.4

x [m]

0.8

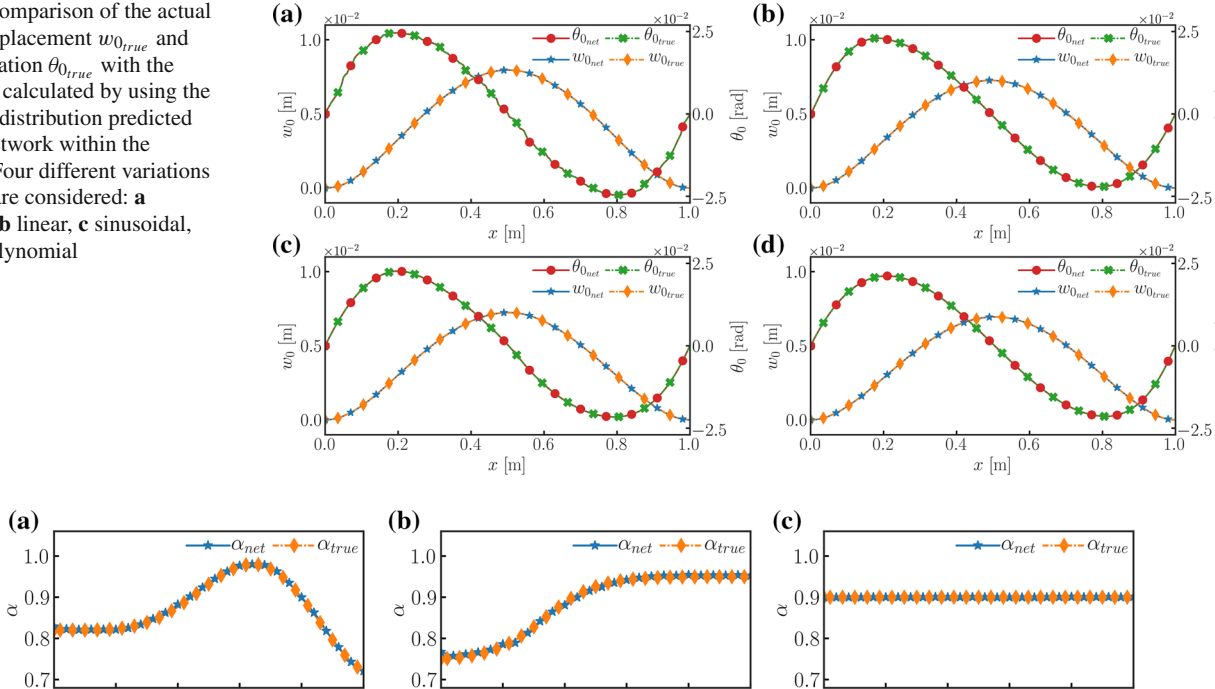


Fig. 9 Network predicted VO (α_{net}) distribution along beam axis for sample problems 5–7 compared with actual fractional-order distribution α_{true} : **a** Bessel $\alpha(x)$, **b** hyperbolic tangent $\alpha(x)$, **c** constant $\alpha(x)$

0.4

x [m]

0.8

1.0

0.2

0.0

obtained the results from $N_s = \{5, 10, 20\}$ sets of measurements. Each set of measurements was obtained by taking samples from the noise probability density functions of w_0 and θ_0 , and then adding them to the nodal values of the corresponding fields. The results for this analysis are presented in Figs. 10-13. In each case, we present the mean value of network predictions (labeled as α_{net}), calculated over the measurements, as well as the 95% confidence bands (represented by the shaded green regions).

Results indicate that the network can closely predict the trend in the VO profile and exhibits significant tolerance to the noise added to the input. The accuracy of the prediction decreases as the amplitude and standard deviation of the noise probability density function are increased. Further, the overall accuracy of the predictions increases proportionally with the number of measurements. In each case, the largest error in the VO prediction always occurs for the random variation (see Fig. 10). This is not surprising because the network is

0.2

0.4

x [m]

0.8



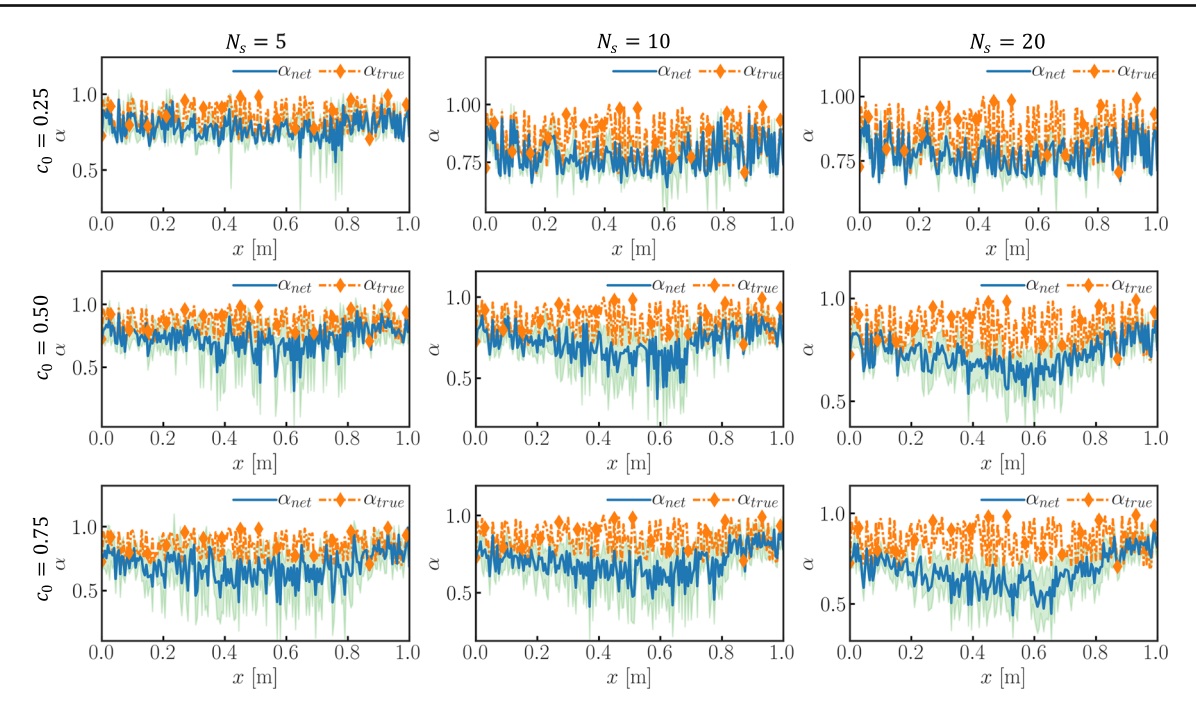


Fig. 10 The mean VO predicted by the network (α_{net}) using noisy data is compared to the true value (α_{true}) . Results are obtained for the random variation of α_{true} , with different number of measurement samples (N_s) and different values of c_0 . The green shaded area shows the 95% confidence bands

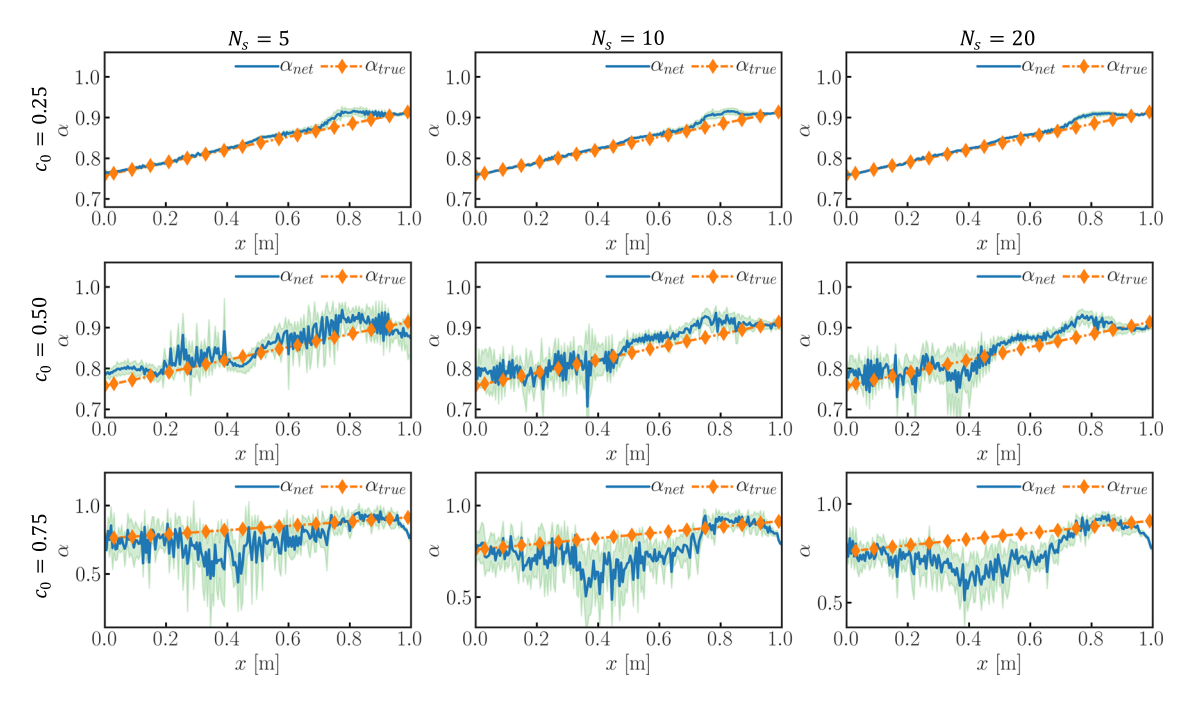


Fig. 11 The mean VO predicted by the network (α_{net}) using noisy data is compared to the true value (α_{true}) . Results are obtained for the linear variation of α_{true} , with different number of measurement samples (N_s) and different values of c_0 . The green shaded area shows the 95% confidence bands



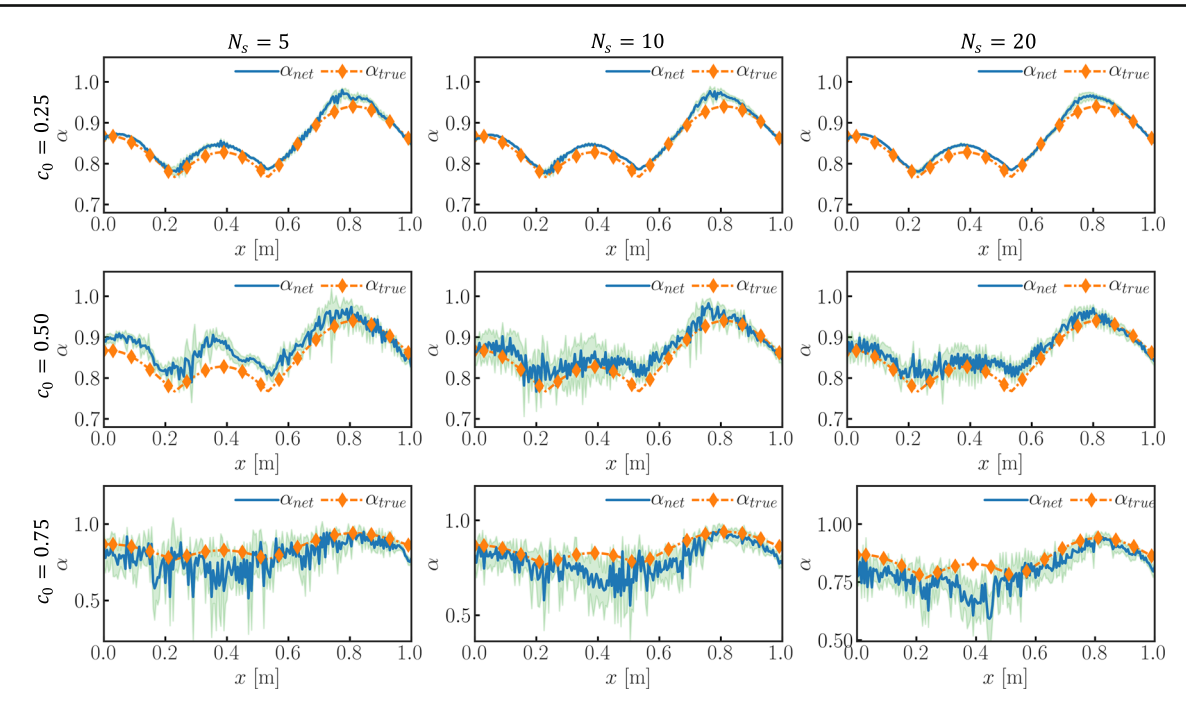


Fig. 12 The mean VO predicted by the network (α_{net}) using noisy data is compared to the true value (α_{true}) . Results are obtained for the sinusoidal variation of α_{true} , with different number of measurement samples (N_s) and different values of c_0 . The green shaded area shows the 95% confidence bands

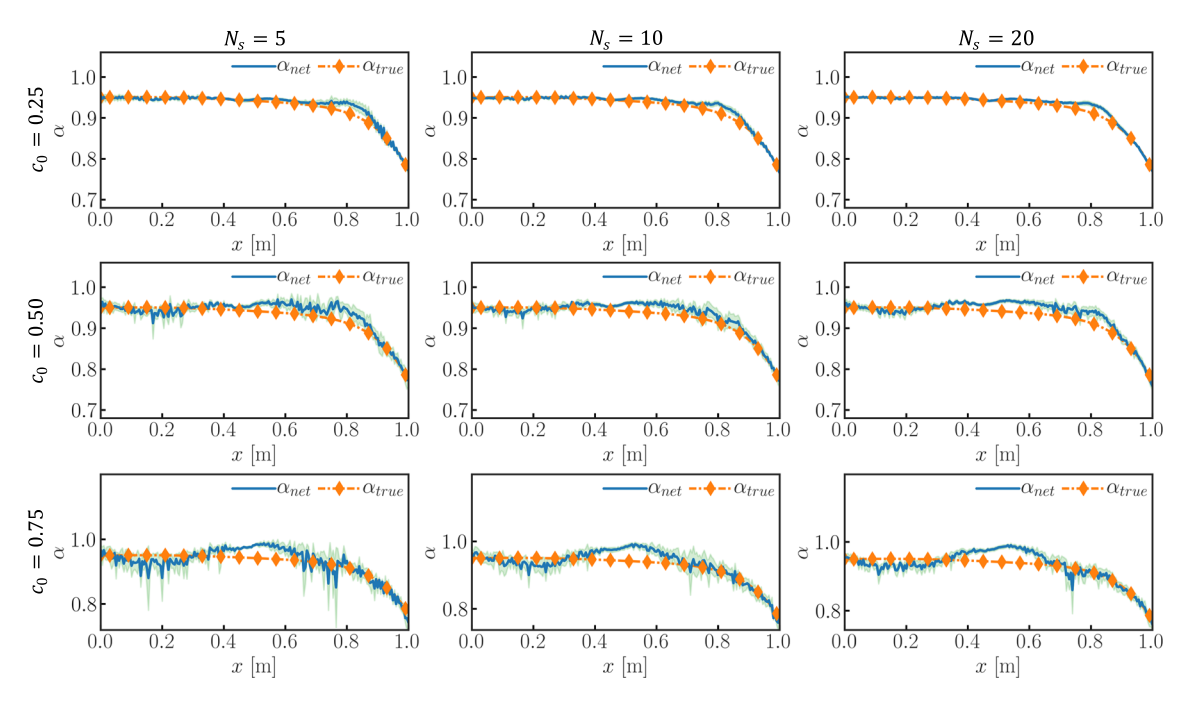


Fig. 13 The mean VO predicted by the network (α_{net}) using noisy data is compared to the true value (α_{true}). Results are obtained for the polynomial variation of α_{true} , with different number of measurement samples (N_s) and different values of c_0 . The green shaded area shows the 95% confidence bands



not provided any specific information to distinguish whether the fluctuations in the response fields are due to measurement noise or due to random changes in VO. In this regard, some additional aspects should be noted in order to put the results into perspective. First, the random distribution of VO does not necessarily reflect a practical scenario and it was chosen to illustrate the flexibility of the network. In fact, we have shown in Sect. 6 that the VO profile that characterizes the response of beams with random distributions in porosity or modulus of elasticity, are not random in nature. Second, if additional information about the system was available a priori, better performance of the network in the presence of noise could still be possible. A possible example includes the case in which the order follows a distinct distribution different from that of the noise; in this latter case, the network could be trained to recognize and separate the effect of different distributions.

Note that, in generating the above predictions, raw unprocessed data was input to the network and, more importantly, the network was not trained a priori with noisy data. Parameter estimations based on traditional inverse techniques, not conditioned a priori on noisy data, generally diverge when provided raw unprocessed signals as input data (since the resulting inverse problems tend to be ill-posed) [62,63]. In this regard, our network exhibits reasonably good performance, since it captures the VO trend accurately with significant confidence. Certainly, the performance of the network can still be improved by leveraging recent developments in network based inverse techniques (e.g. by casting the inverse problem within a Bayesian framework [63,64]). However, in order to limit the focus of this study to the formulation, physical interpretation, and applications of the VO approach to nonlocal elasticity, we avoided these additional investigations and merely established that the presence of noise does not corrupt or impede the prediction of the developed network.

6 Practical applications of variable-order continuum theory

As discussed in Sect. 2, the VO fractional continuum model is particularly well suited to model complex systems exhibiting position-dependent behavior. In the present study, where particular emphasis is given to modeling nonlocality, the VO $\alpha(x)$ captures the position-dependent strength of the nonlocal behavior. In order to further emphasize this aspect, we used the VO formulation and the neural network approach to show the potential of the method for applications to the static response of two different types of heterogeneous beams with spatially varying properties: (1) porous beams with spatially varying degree of porosity, and (2) functionally graded beams with spatially varying modulus of elasticity. Results

show that the VO approach can accurately capture this complex system behavior.

6.1 Static analysis of porous beams

In this section, we show how the VO formulation can be instrumental in the accurate and computationally efficient analysis of porous structures (in this case beams) with spatially varying degree of porosity. Indeed, the spatially varying degree of non-locality which can be effectively captured by the VO $\alpha(x)$ formulation. As mentioned previously in the introduction, we will establish this capability of the VO framework concretely, by using either a direct comparison of the VO predictions against a full 3D finite element solution or predictions made via a commonly adopted classical (integer-order) homogenization scheme.

Before presenting the response of the porous beams obtained via the aforementioned techniques, we first discuss the algorithm adopted for the generation of the porous beam:

- 1. First, the volume of dimensions $L \times b \times h$ (see Table 1) was divided into a 3D array consisting of $N_x \times N_y \times N_z$ points. Then, a numerical value in the range [0, 1] was randomly extracted from a Gaussian distribution and assigned to each physical point. Finally, a Gaussian filter with a predefined standard deviation was applied to the 3D array and all points with values above a pre-defined and fixed constant (say, p_0) were identified as points that make up the porous beam. In other terms, the 3D array of random numbers in the range [0, 1] (obtained after the application of the Gaussian filter) was converted into a binary array with the points identified by the value 1 forming the porous beam. It immediately follows that the fixed constant p_0 is equal to the net porosity of the beam. Note also that the standard deviation of the Gaussian filter, applied previously, determines the size of the pores in the beam. The porous beam generated from the above steps can be visualized as a level-set of grid-points assigned with the value 1 (see, for example, Fig. 14).
- 2. The porous beam, generated at the previous step, was included in a rectangular shell as illustrated in Fig. 14 and labeled "outer shell". Numerically, this is achieved by padding the 3D array, obtained at the end of the previous step, by layer of 1, at the desired locations. For all the porous beams considered in this study, the thickness of the rectangular shell was set at 5 mm, and its introduction results in a decrease in the net porosity of the beam by 0.04 units. From a practical perspective, this process results in the formation of a sandwiched beam structure with a porous core. The outer flat surfaces provide ease of application of the external loads and boundary constraints, regardless of a numerical or an experimental setting.



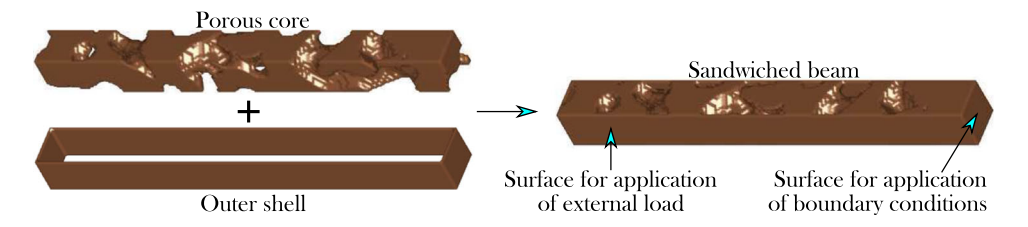


Fig. 14 Schematics of the sandwich beam with porous core used as benchmark structure to test the VO approach. The beam is obtained by enclosing a porous core in a rectangular outer shell. The flat outer shell also simplifies the application of external loads and boundary conditions

Different examples of porous beams having a net porosity increasing from $p_0 = 0.18$ to $p_0 = 0.24$ in steps of $\Delta p_0 =$ 0.02, can be found in Figs. 15a-19a. In each figure, we have presented only the porous core for better visualization of the spatial distribution of pores. It appears also that each beam can be seen as a collection of sections perpendicular to the mid-plane (or mid-axis), such that the porosity of each section is a random number within the interval [0, 1]. More specifically, the porosity of these planes perpendicular to the mid-plane of the beam can be identified as a function $p_0(x)$. The complement of the porosity function, that is p(x) = $1 - p_0(x)$, is used to characterize each beam as shown in Figs. 15b–19b. The function p(x) determines the amount of material present within each plane perpendicular to the midplane of the beam, and it is a key quantity to be used in the integer-order (IO) homogenization scheme described in the following.

The static responses of the porous beams were obtained by applying a UDTL and clamped boundary conditions at both their ends. Note that the loading conditions are identical to that assumed previously in the problem definition (in Sect. 4.1). Three different approaches were adopted in order to obtain the static response:

- 3D finite element analysis (FEA) was performed by using the commercial finite element software COMSOL Multiphysics. In order to perform the 3D FEA in COMSOL, the 3D binary array describing the porous geometry (generated at the end of the previously outlined algorithm) was converted into a stereolithography (STL) file, using the standard marching cubes algorithm [65,66]. COMSOL functionalities were then used to extract the geometry, mesh the solid, and perform the FEA
- *VO nonlocal elasticity framework* the neural network methodology was used to predict the VO $\alpha(x)$ characterising the static responses of the porous beams. The VO $\alpha(x)$ corresponding to the different porous beams are presented in the Fig. 15b Fig. 19b. The VO $\alpha(x)$ was used within the VO f-FEM (see Sect 4.2) to simulate the responses of the porous beams.

• Integer-order homogenization – the porous beam was modeled as a solid (that is p(x) = 1) anisotropic beam with a spatially varying modulus of elasticity given as $E(x) = [(1-p_0(x)]E_0 \equiv p(x)E_0$, where E_0 is the modulus of elasticity of the solid used to construct the porous beam (see Table 1). The spatially varying E(x) was then used within the classical IO Euler-Bernoulli beam formulation to simulate the response of the porous beams. We merely note that, the aforementioned approach is commonly adopted in classical literature to model the response of porous structures [67,68].

In order to enable a comprehensive assessment of the results, it is essential to discuss the factors leading to the selection of the three different models presented above as well as the key highlights of each model. The static deformation of the sandwich porous beam is affected by two key physical mechanisms: (1) the nonlocal interaction between different pores during deformation, and (2) the relation between the strength of this interaction and the spatial distribution of porosity. This position-dependent nonlocal phenomenon results in a position-dependent softening of the beam structure, that is directly related to the distribution and shape of the pores. Consequently, the degree of accuracy of the static response predicted for the porous beams, using the three different approaches enlisted above, is dependent on how each approach accounts for the distribution and shapes of pores in the 3D sandwiched beam.

Following from the above discussion, the 3D FEA will be used as reference solution to assess the performance of the VO and IO approaches. While still being a numerical approximate solution, FEA fully accounts for the 3D distribution of porosity within the beam and hence, within the chosen level of spatial discretization, it can be considered as a reliable approximation of the detailed 3D continuous porous geometry. In the VO approach, the 3D distribution of porosity is captured by the VO $\alpha(x)$, hence providing a homogenized representation of the initial 3D system. From a geometrical perspective, the information on the spatial distribution of porosity is lost in this 1D abstraction. However, from a physical perspective, the underlying position-dependent non-locality resulting from the interaction between the pores and



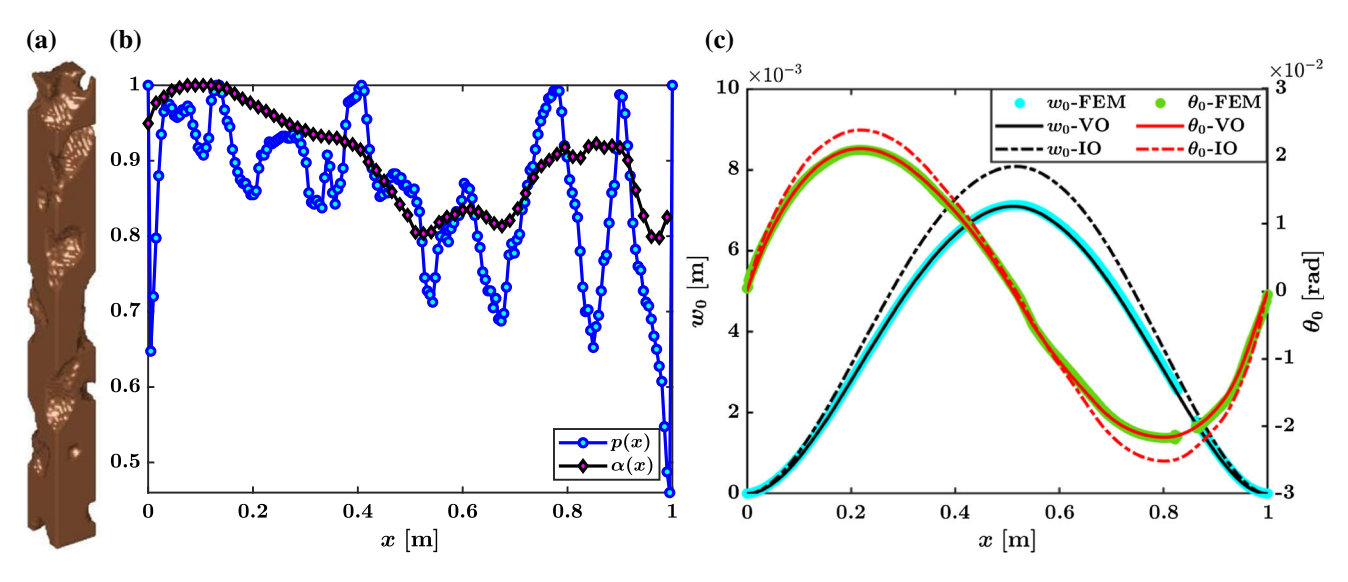


Fig. 15 a Example of porous core with net porosity 0.18. b The spatial distribution of the sectional porosity and of the VO across the length of the beam. c The static response of the beam obtained by employing the three different methods: 3D FEA, VO formulation, and the IO homogenization method

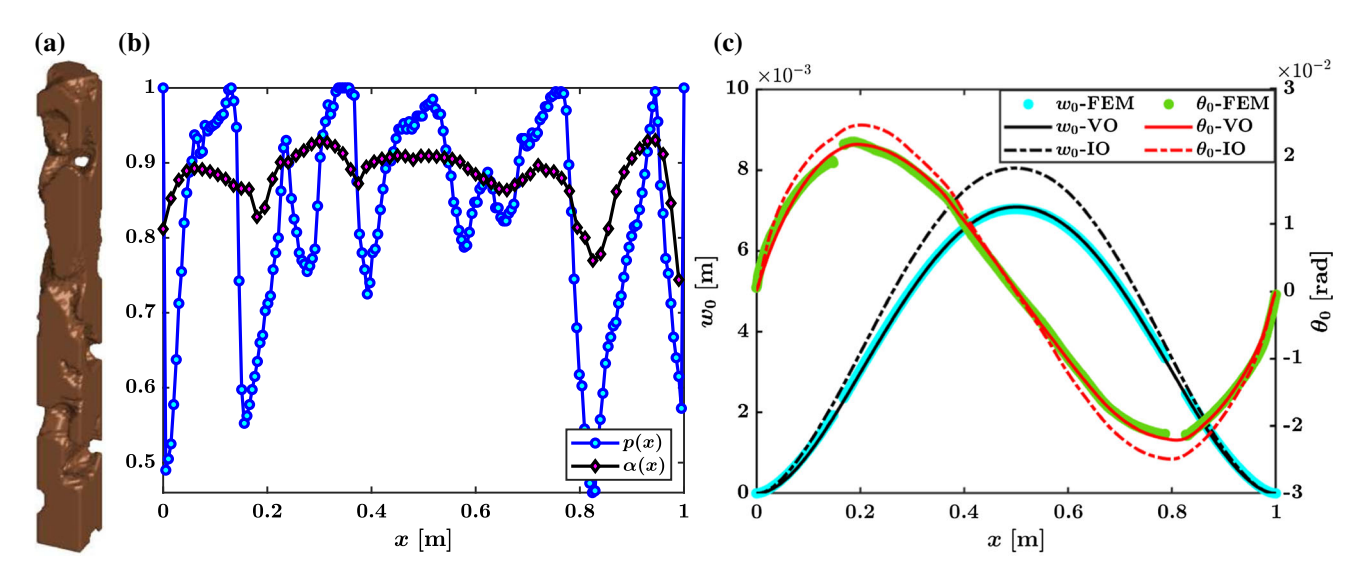


Fig. 16 a Example of porous core with net porosity 0.2. b The spatial distribution of the sectional porosity and of the VO across the length of the beam. c The static response of the beam obtained by employing the three different methods: 3D FEA, VO formulation, and the IO homogenization method

their spatial distribution, is captured by the differ-integral and position-dependent nature of the VO fractional operators. We will show, by means of numerical results, that the VO approach combines the computational efficiency of a reduced-order model with a high-level accuracy close to a full size 3D continuum model. Finally, note that the IO homogenization approach merely accounts for the presence and spatial distribution of pores by *locally* softening the beam via the spatially varying modulus of elasticity E(x). Due to the use of IO operators, the IO approach does not capture the underlying nonlocal phenomenon (and hence, its position-dependent strength as well) resulting from the interaction

between the spatially distributed pores. Hence, a significant part of the information available in the original 3D representation of the system is lost when modeling the porous beam by using the IO approach. In fact, the IO approach was chosen to contrast and further highlight the advantage of VO fractional mechanics, over classical IO mechanics, in modeling systems with complex heterogeneous features that result in non-classical manifestations of local microstructural information at the continuum level. With the above understanding, we proceed to compare the predictions of the three different approaches.



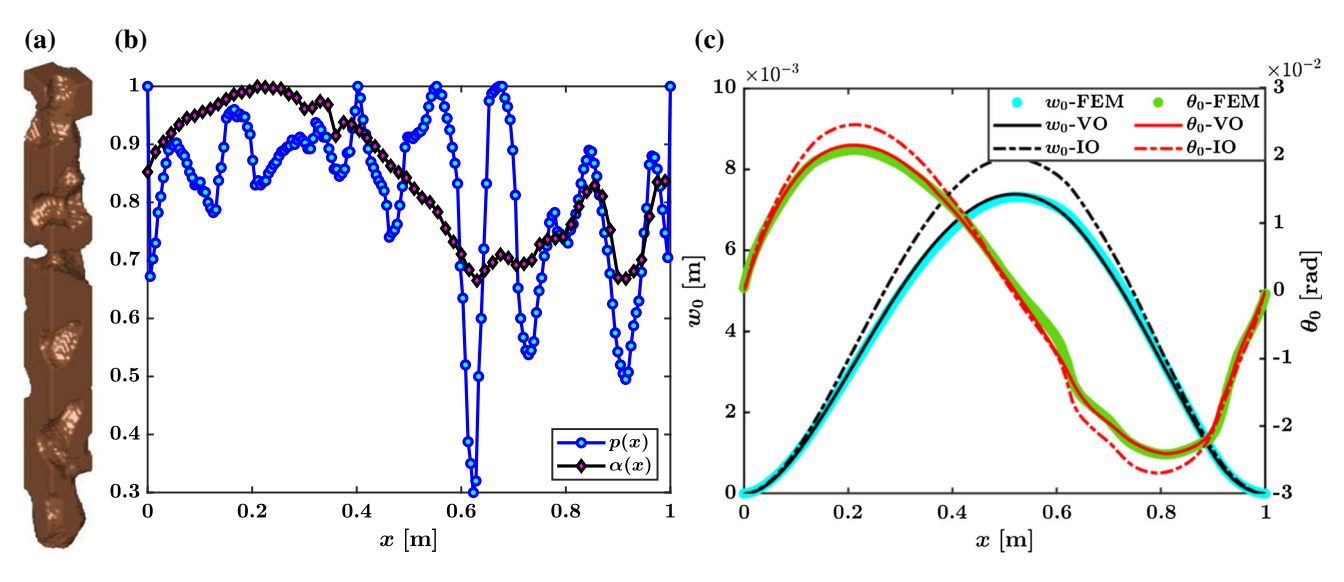


Fig. 17 a Example of porous core with net porosity 0.22. b The spatial distribution of the sectional porosity and of the VO across the length of the beam. c The static response of the beam obtained by employing the three different methods: 3D FEA, VO formulation, and the IO homogenization method

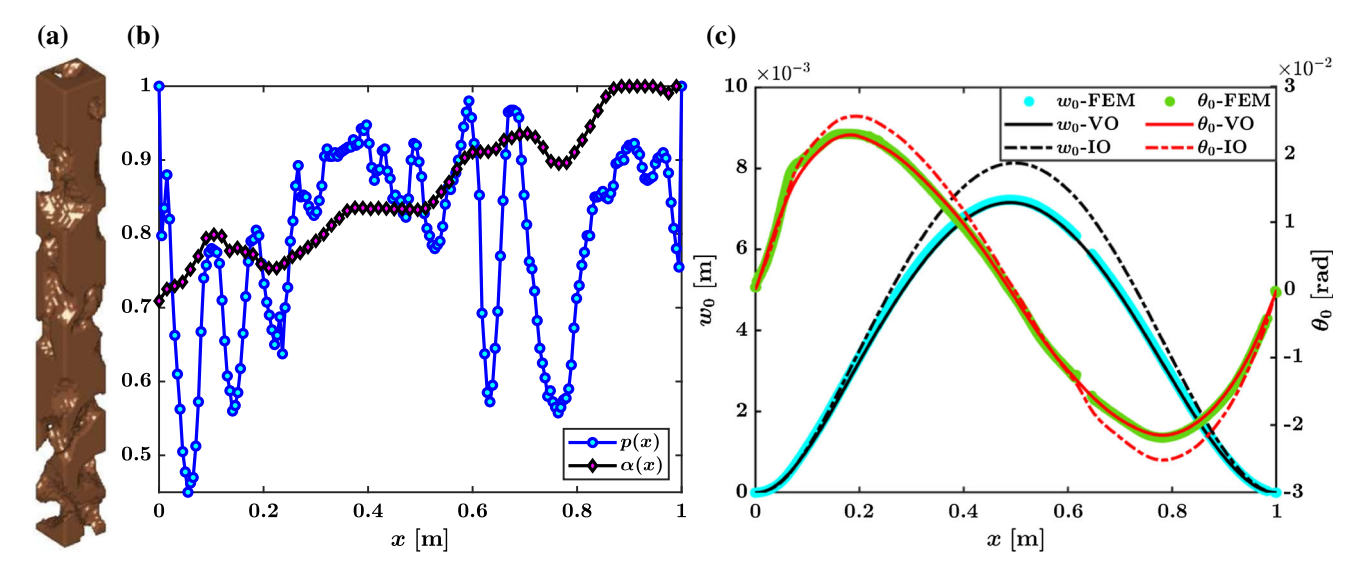


Fig. 18 a Example of porous core with net porosity 0.24. b The spatial distribution of the sectional porosity and of the VO across the length of the beam. c The static response of the beam obtained by employing the three different methods: 3D FEA, VO formulation, and the IO homogenization method

The static responses of the porous beams, in terms of the transverse displacement $(w_0(x))$ and rotation of the transverse normals $\theta_0(x)$ of the symmetry axis of the geometric mid-plane $(\forall x \cup \{y,z\} = 0)$, via the above described approaches are compared in Figs. 15c–19c. The apparent discontinuity in the response of porous beams predicted via 3D FEA (except for the porous beam with $p_0 = 0.22$) is due to the fact that some pores overlap with the symmetry axis of the beam, hence a nodal displacement cannot be directly extracted. The total number of degrees of freedom and the run-time taken by each simulation to achieve a *fully converged solution* are summarized in Table 4. We selected a convergence criterion based on the difference of

both the displacement and the rotation fields between successive refinements; an arbitrary threshold of 2% was chosen for this parameter. Further, the time consumed in each case is taken as the average of 3 successive runs for the 3D FEA and as the average of 10 successive runs for the VO and IO homogenized approaches. Note that the total time presented for the VO and IO approaches also includes the time employed to generate the VO $\alpha(x)$ by the trained network, and the homogenized modulus of elasticity E(x), respectively. All the simulations were run on a personal computer equipped with an Intel(R) Core(TM) i7-1065G7 processor and 8.00 GB RAM.



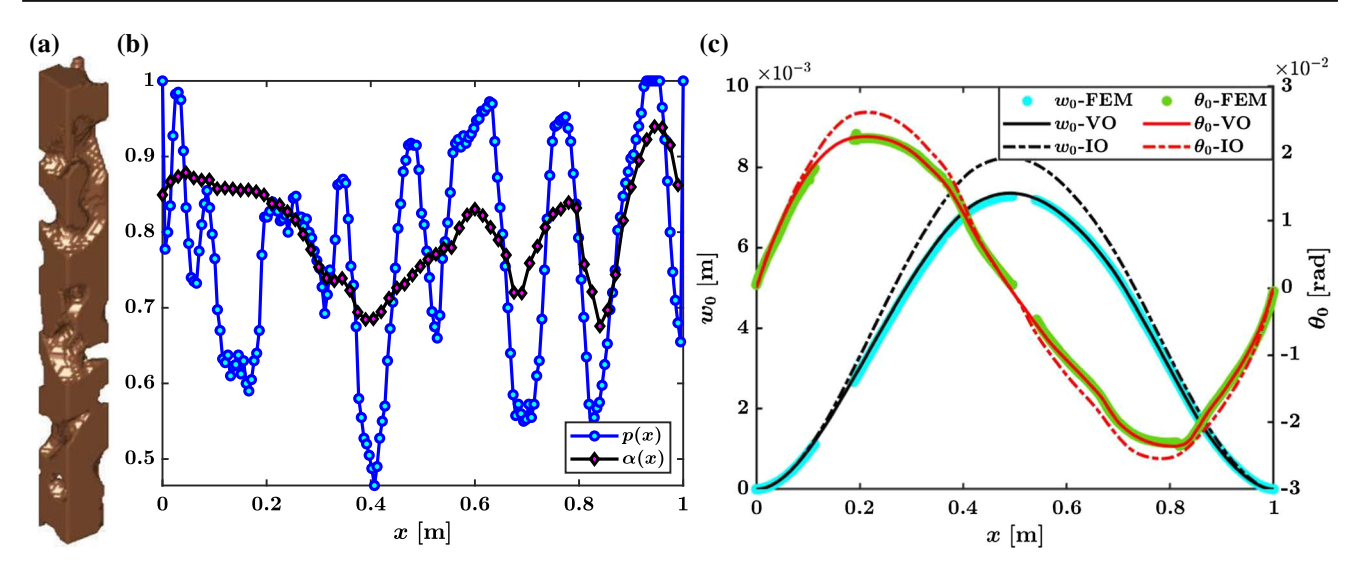


Fig. 19 a Example of porous core with net porosity 0.26. **b** The spatial distribution of the sectional porosity and of the VO across the length of the beam. **c** The static response of the beam obtained by employing the three different methods: 3D FEA, VO formulation, and the IO homogenization method

Table 4 Comparison of the total number of degrees of freedom (N_{DOF}) and average computational time (T_s) required to achieve a converged static response with the three different modeling approaches and for different levels of porosity p_0

	p_0	0.18	0.20	0.22	0.24	0.26
N_{DOF}	FEA	1.67×10^{6}	1.58×10^{6}	1.64×10^{6}	2.04×10^{6}	1.98×10^{6}
	VO	6×10^2				
	IO	6×10^2				
T_s [s]	FEA	1800	1260	1320	1860	1980
	VO	4.0	4.0	4.0	4.0	4.0
	IO	2.0	2.0	2.0	2.0	2.0

The results presented in Figs. 15c-19c and Table 4 demonstrate the accuracy and superior computational efficiency of the VO framework. The spatial error distribution along the coordinate x for the VO and IO approaches is defined as:

$$Er(x) = \frac{w_{\square}(x) - w_{3D}(x)}{w_{3D}(x)} \times 100$$
 (28)

In the above equation, Er(x) denotes the error at point x, $w_{\square}(\square \in VO, IO)$ denotes the transverse displacement at point x obtained by using either the VO or IO approach, and w_{3D} denotes the benchmark solution obtained via 3D FEA. The error in the predictions obtained from the VO and IO approaches, with respect to the benchmark 3D FEA solution, is presented in Fig. 20. While the IO approach leads to an error as high as 15% in predicting the maximum transverse displacement of the porous beams, the corresponding error in the VO solution is less than 2% in all the cases. In fact, the VO approach is highly accurate when compared to the IO approach for points (x) farther from the boundaries $(x \in [0.2L, 0.8L])$. For points close to the boundary $(x \in (0, 0.05L] \cup [0.95L, L))$, a large error is observed for both the approaches due to very small values of the displace-

ment and the difference in the significant digits used in VO f-FEM, IO FEM, and COMSOL simulations. It follows that the error fraction defined in Eq. (28) is very ill-conditioned close to the boundaries. Note that, rounding-off the displacement values obtained via the three different approaches, to a common number of significant digits, leads to an artificial zero error near the boundaries. From a practical perspective, the large error localized near the boundaries does not hold much relevance, since the maximum displacement value within this region is significantly small (at least 20 times smaller that the maximum displacement of the beam) to drastically alter outcomes in a real-world scenario. Apart from being highly accurate, the VO framework enables a significantly faster approach when compared to 3D FEA. More specifically, the VO approach is at least 315 times faster than the 3D FEA approach, as observed for the porous beam with $p_0 = 0.20$. Further, the ability of the VO approach to achieve an accurate and converged solution with significantly lower number of degrees of freedom, when compared to the fully 3D finite element approach, also suggests a conspicuous reduction in the computational complexity upon adopting the VO approach. This latter aspect also highlights the unique potential of the VO approach in achieving reduced-order models or well-



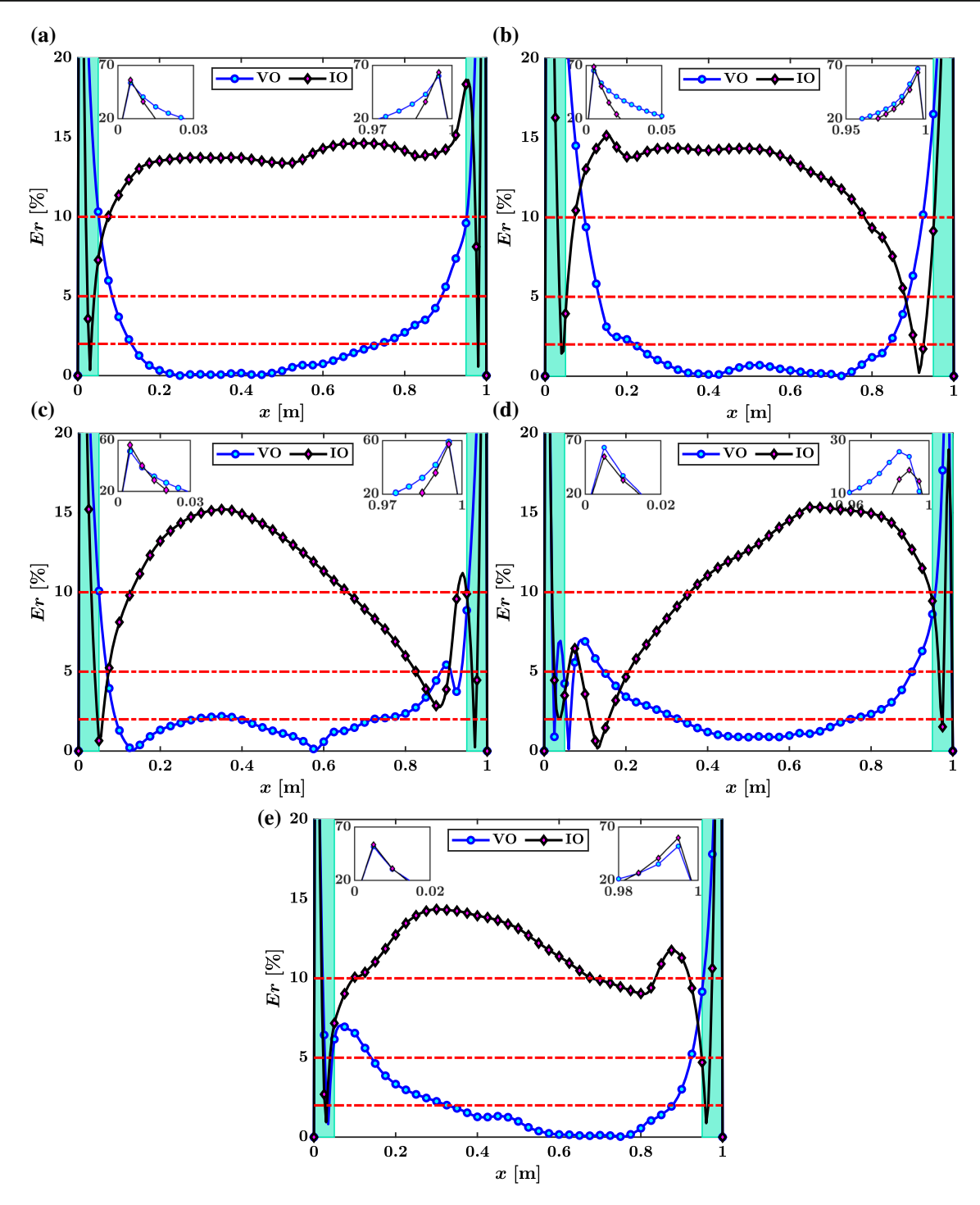


Fig. 20 Error in the predictions of the VO and IO approaches with respect to the 3D FEA prediction for the porous beams with net porosity: ${\bf a}~p_0=0.18$, ${\bf b}~p_0=0.20$, ${\bf c}~p_0=0.22$, ${\bf d}~p_0=0.24$, and ${\bf e}~p_0=0.26$. The three horizontal dashed-dotted lines denote Er=2%, Er=5%, and Er=10%. As evident, the VO approach is highly

accurate when compared to the IO approach for points (x) farther from the boundaries $(x \in [0.2L, 0.8L])$. For points close to the boundary, a large error (see the insets within each sub-figure) is observed due to very small values of displacement and difference in the significant digits used in VO f-FEM, IO FEM and COMSOL simulations



posed homogenization approaches, for describing the effect of microstructural inhomogeneities present within complex solids, on a global scale. In this regard, although we considered a relatively simple beam structure in this study, it can be envisioned that the VO framework has significant potential in reducing the typically high computational costs incurred in the simulation of complex porous structures as well as their assemblies.

6.2 Static analysis of functionally graded beams

In order to illustrate further possible applications of the VO nonlocal elasticity framework, we apply the methodology to model the static response of functionally graded beams. Contrary to the modeling of porous beams, which offered a very direct and practical interpretation, the simulations presented here below will be tackled from a more numerical perspective. This choice was made to illustrate the flexibility of the method and its possible application to classes of continuum mechanics problems characterized by functionally graded properties. Nonetheless, all the results will confirm the same underlying property of the VO framework that is its ability to accurately capture position-dependent nonlocal behavior.

From a broad perspective, the spatially varying elastic properties in functionally graded beams result in a spatially-dependent nonlocal effect which can be encoded into the VO $\alpha(x)$. In order to demonstrate this aspect, we consider two different heterogeneous beams with: (1) a random gradation, and (2) a linear gradation in the modulus of elasticity across the length of the beam. The variation of the modulus of elasticity in these different beams is schematically illustrated in Figs. 21b and 22b. The figures also present the variation of the modulus of elasticity ($\overline{E}(x)$) non-dimensionalized with respect to the modulus of elasticity of the isotropic beam (with $E_0 = 30$ MPa, see Table 1). For the random gradation, $\overline{E}(x)$ was extracted from a uniform distribution within the interval [0.8, 1]. The linear gradation was set as:

$$\overline{E}(x) = 0.8 + 0.2x \tag{29}$$

Note that the position-dependent variation in the elastic properties could result from several underlying physical mechanisms such as, for example, material heterogeneity, and the presence of thermal gradients, as also mentioned previously. In fact, the nucleation and evolution of microstructural damage can also lead to functional gradations in the material elastic properties. As an example, in the linearly graded beam, one can envision a pre-existing damage resulting in a progressive softening of the beam towards the boundary at x = 0.

As for the porous beams, the functionally graded beams were clamped at both ends and subjected to a UDTL. The

responses of the functionally graded beams are obtained via the classical FEA and the VO beam theory. While the classical FEA accounts for the spatially varying elastic modulus, the VO beam theory uses an isotropic (homogenized) beam with elastic modulus $E_0 = 30$ MPa. The VO $\alpha(x)$ characterizing the responses of the functionally graded beams was obtained via the trained network and presented in Figs. 21b and 22b. The response obtained for each beam, following the two different approaches, are compared in Figs. 21c and 22c. As expected, the match between the FEA and VO results is excellent. Note that, unlike the analysis of porous beams, we do not model the responses of the functionally graded beams using an IO homogenization approach. Indeed, functionally graded beams are typically analyzed in literature via classical IO approaches to nonlocal elasticity. Recall that a key limitation of the classical nonlocal approaches consists in their inability to yield a positive-definite strain energy density. In order to achieve a positive-definite total strain energy, the classical IO approaches require a symmetric nonlocal kernel [11,54]. This latter condition prevents the application of the resulting theory to the analysis of structures exhibiting asymmetric long-range interactions resulting from, as an example, material heterogeneity, thermal gradients, structural porosity, microstructural damage or even due to asymmetric engineered nonlocality [20,53,69–71]. In fact, the misuse of classical nonlocal approaches to model structures made from functionally graded materials was highlighted very recently in [49]. Consequently, we did not model the functionally graded beams by any classical IO approach.

7 Conclusions

The key contributions of this study are four-fold. First, we developed the variable-order (VO) approach to nonlocal elasticity. Second, we specialized this formulation to the static analysis of nonlocal slender beams. Next, we developed a deep learning strategy to extract the VO pattern in cases when only the response of the nonlocal solid is available. Finally, we presented the application of the developed VO framework to the static analysis of porous and functionally graded beams. The VO approach to elasticity captures a spatially-dependent degree of nonlocality across the nonlocal solid and provides the flexibility to account for either spatially varying horizon of nonlocality or possible asymmetry in the horizon. The VO formulation adopts a physically consistent fractional-order kinematics that ensures a positive-definite and self-adjoint system. These characteristics guarantee well-posedness of the governing equations derived via variational minimization of the potential energy. Consequently, the VO formulation is free from inconsistent predictions, characteristic of classical nonlocal



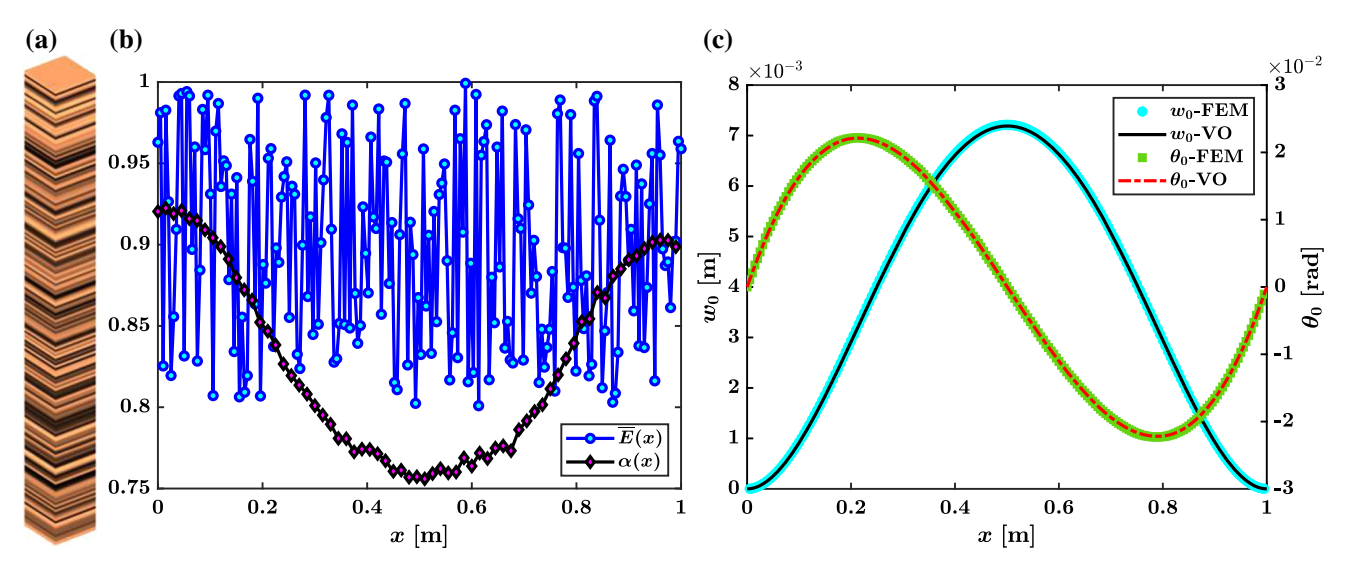


Fig. 21 a Schematic of a heterogenous beam with a random gradation in the modulus of elasticity. b The spatial distribution of the modulus of elasticity and of the VO across the length of the beam. c The static response of the beam obtained from 3D FEA and the VO formulation

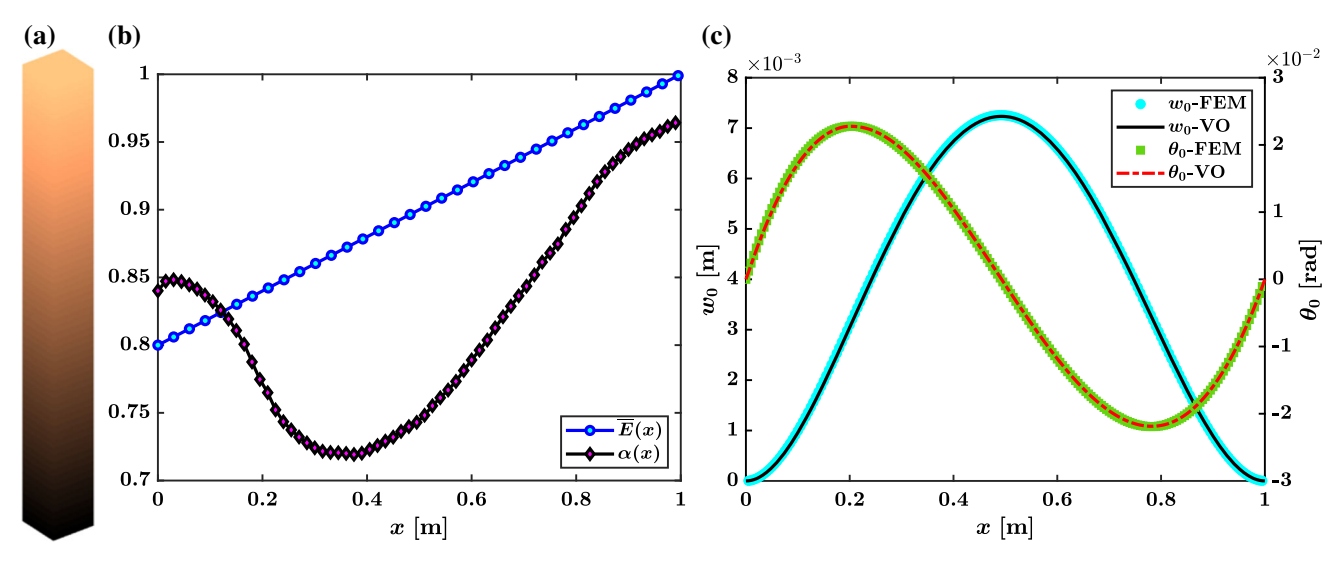


Fig. 22 a Schematic of a heterogenous beam with linear gradation in the modulus of elasticity. b The spatial distribution of the modulus of elasticity and of the VO across the length of the beam. c The static response of the beam obtained from 3D FEA and the VO formulation

integral formulations under certain boundary and loading conditions.

The well-posed nonlocal formulation enables the development of a deep learning based technique to address the inverse problem consisting in the determination of the VO distribution describing the response of a nonlocal beam. This latter contribution of our study addresses a major challenge in the promotion and diversification of the applications of fractional calculus to the modeling of physical systems, that is the determination of the fractional-model parameters. The proposed method leverages the outstanding computational efficiency of trained neural networks to estimate the VO distribution of a nonlocal solid medium based on its measured response. Accurate solutions to this complex

form of inverse problem were achieved by exploiting the unique features of deep bidirectional recurrent neural networks (BRNN). Different VO patterns, either consistent or inconsistent with the training data, were simulated and successfully identified. Finally, the proposed framework was applied to the simulation of the static response of porous and functionally graded beams with complex spatial distributions of the corresponding material properties. These applications concretely established the ability of the VO framework to perform reduced-order multiscale predictions with accuracy comparable to high-fidelity 3D finite element models, albeit requiring significantly smaller computational resources. While the present framework was developed and validated for the case of nonlocal beams, the methodology



is general and can be easily extended to higher dimensional problems. In conclusion, the physically consistent and well-posed VO approach to nonlocal continua combined with deep learning techniques for fractional parameter estimation provide a critical step to further establish and extend fractional-order continuum mechanics approaches to modeling the response of real-world complex structures.

Acknowledgements The authors gratefully acknowledge the financial support of the National Science Foundation (NSF) under Grants MOMS #1761423 and CAREER #1621909, and the Defense Advanced Research Project Agency (DARPA) under Grant #D19AP00052. The content and information presented in this manuscript do not necessarily reflect the position or the policy of the government. The material is approved for public release; distribution is unlimited.

Declarations

Conflict of interest The authors declare no competing interest.

Appendix

A: Definitions of variable-order fractional derivatives

Variable-order fractional operators were first conceptualized by Samko et al. [29] in 1993 as a natural extension of CO fractional operators. Over time, researchers have presented several definitions of VO fractional derivatives. The most significant discriminant factor, between the different definitions, consisted in the memory behavior of the operator. A detailed review of the different definitions, properties, and their applications can be found in [37,72]. Here below, we report the definitions of the type-I and type-II VO Caputo operators that have been used in this work.

Type-I: If f(x) and $\alpha(x)$ are continuous real-valued functions on (a,b), the left- and right-handed VO Caputo derivative to the order $\alpha(x) > 0$ with *no order-memory* are defined as:

Left-handed derivative:
$${}_{a}^{C} D_{x}^{\alpha(x)} f(x)$$

$$= \frac{1}{\Gamma(n - \alpha(x))} \int_{a}^{x} \frac{D_{x'}^{n} f(x')}{(x - x')^{1 + \alpha(x) - n}} dx'$$
(30a)

Right-handed derivative: ${}_{x}^{C}D_{b}^{\alpha(x)}f(x)$

$$= \frac{(-1)^n}{\Gamma(n-\alpha(x))} \int_x^b \frac{D_{x'}^n f(x')}{(x'-x)^{1+\alpha(x)-n}} dx'$$
 (30b)

where $n = \lceil \alpha(x) \rceil$ is the upper integer bound on $\alpha(x)$ at the spatial location x, $\Gamma(\cdot)$ is the Gamma function, and x' is a dummy spatial variable of integration. As discussed in Sect. $2 \alpha(x) \in (0, 1)$ throughout this work. Under this latter

condition, the expressions in Eq. (30) can be simplified as:

Left-handed derivative: ${}_a^C D_x^{\alpha(x)} f(x)$

$$= \frac{1}{\Gamma(1 - \alpha(x))} \int_{a}^{x} \frac{D_{x'}^{1} f(x')}{(x - x')^{\alpha(x)}} dx'$$
 (31a)

Right-handed derivative: ${}_{x}^{C}D_{h}^{\alpha(x)}f(x)$

$$= \frac{-1}{\Gamma(1 - \alpha(x))} \int_{x}^{b} \frac{D_{x'}^{1} f(x')}{(x' - x)^{\alpha(x)}} dx'$$
 (31b)

Analogous expressions can be obtained for the Type-II and Type-III operators presented in the following when $\alpha(x) \in (0, 1)$. We do not provide them here for the sake of brevity.

Type-II: If f(x) and $\alpha(x)$ are continuous real-valued functions on (a,b), the left- and right-handed VO Caputo derivative to the order $\alpha(x) > 0$ with *weak order-memory* are defined as:

Left-handed derivative:
$${}_{a}^{C}D_{x}^{\alpha(x')}f(x)$$

$$=\int_{a}^{x}\frac{1}{\Gamma(n-\alpha(x'))}\left[\frac{D_{x'}^{n}f(x')}{(x-x')^{1+\alpha(x')-n}}\right]\mathrm{d}x' \qquad (32a)$$

Right-handed derivative: ${}_{x}^{C}D_{b}^{\alpha(x')}f(x)$

$$= \int_{x}^{b} \frac{(-1)^{n}}{\Gamma(n - \alpha(x'))} \left[\frac{D_{x'}^{n} f(x')}{(x' - x)^{1 + \alpha(x') - n}} \right] dx'$$
 (32b)

Type-III: If f(x) and $\alpha(x)$ are continuous real-valued functions on (a, b), the left- and right-handed VO Caputo derivative to the order $\alpha(x) > 0$ with *weak order-memory* are defined as:

Left-handed derivative:
$${}_{a}^{C}D_{x}^{\alpha(x-x')}f(x)$$

$$=\int_{a}^{x}\frac{1}{\Gamma(n-\alpha(x-x'))}\left[\frac{D_{x'}^{n}f(x')}{(x-x')^{1+\alpha(x-x')-n}}\right]dx'$$
(33a)

Right-handed derivative: ${}_{x}^{C} D_{b}^{\alpha(x-x')} f(x)$

$$= \int_{x}^{b} \frac{(-1)^{n}}{\Gamma(n - \alpha(x - x'))} \left[\frac{D_{x'}^{n} f(x')}{(x' - x)^{1 + \alpha(x - x') - n}} \right] dx'$$
(33b)

Note the differences within the definitions of the different VO derivatives. While the strength of the power-law kernel, that is the exponent of the denominator, is fixed for the point x for the type-I derivative, the strength of the type-II kernel is a function of the dummy variable x' and the strength of the type-III kernel a function of the relative separation between x and x'. This is exactly the reason which leads to difference in the memory characteristics of the different definitions. Detailed discussions on the properties of these derivatives, including linearity, time invariance, memory characteristics (both operator- and order-memory), Laplace transforms, and physical realization using switches can be found in [30].



B: Frame-invariance of the VO continuum model - Type-I v/s Type-II v/s Type-III operators

In the following, we will analyze the frame-invariance of the variable-order continuum formulation resulting from the use of either type-I or type-II or type-III VO Caputo derivatives. Consider a rigid-body motion superimposed on a general point \boldsymbol{X} (see Fig. 1a) of the reference configuration of the body as:

$$\Psi(X,t) = \mathbf{c}(t) + \mathbf{Q}(t)X, \tag{34}$$

where $\mathbf{Q}(t)$ is a proper orthogonal tensor denoting a rotation and $\mathbf{c}(t)$ is a spatially constant term representing a translation. Under this rigid-body motion, the fractional deformation gradient tensor denoted as $\tilde{\mathbf{F}}_X^{\Psi}$ should be an orthogonal tensor such that $\tilde{\mathbf{F}}_X^{\Psi T} \tilde{\mathbf{F}}_X^{\Psi} = \mathbf{I}$. More specifically, the fractional deformation gradient tensor should transform as $\tilde{\mathbf{F}}_X^{\Psi} = \mathbf{Q}$ (similar to the classical continuum case where $\mathbf{F}^{\Psi} = \mathbf{Q}$) such that the strain measures are null. As discussed in detail in [10], the fractional deformation gradient tensor $\tilde{\mathbf{F}}_X^{\Psi}$ is defined as the fractional-order derivative of the motion Ψ with respect to the reference coordinates, that is, $\tilde{\mathbf{F}}_X^{\Psi} = D_X^{\alpha(X,X')}\Psi$.

Type-I derivative: Consider the formulation involving type-I VO derivatives. Recalling the definition of the type-I VO-RC derivative from Eqs. (2,30) it follows that:

$$\tilde{\mathbf{F}}_{X_{ij}}^{\Psi} = \frac{1}{2} \Gamma(2 - \alpha(X)) \left[\frac{L_{-j}^{\alpha(X) - 1}}{\Gamma(1 - \alpha(X))} \int_{X_{-j}}^{X_{j}} \frac{D_{X'_{j}}^{1} \Psi_{i}(X', t)}{(X_{j} - X'_{j})^{\alpha(X)}} dX'_{j} + \frac{L_{+j}^{\alpha(X) - 1}}{\Gamma(1 - \alpha(X))} \int_{X_{j}}^{X_{+j}} \frac{D_{X'_{j}}^{1} \Psi_{i}(X', t)}{(X'_{j} - X_{j})^{\alpha(X)}} dX'_{j} \right]$$
(35)

where X' is the dummy vector representing the spatial variable, and L_{-j} and L_{+j} are the length scales corresponding to the horizon of nonlocality in the reference configuration. $D^1_{X'}\Psi_i(X',t)$ simplifies as:

$$D_{X'_{j}}^{1}\Psi_{i}(X',t) = \frac{d\Psi_{i}(X',t)}{dX'_{i}} = \frac{d}{dX'_{i}}(c_{i} + Q_{ik}X'_{k})$$
 (36)

Noting that $\frac{dc_i(t)}{dX'_j} = 0$ and $\mathbf{Q} = \mathbf{Q}(t)$ it follows that:

$$D_{X'_{i}}^{1}\Psi_{i}(X',t) = Q_{ik}X'_{k,j} = Q_{ik}\delta_{kj} = Q_{ij}$$
(37)

Thus, under the rigid body motion Ψ :

$$\tilde{\mathbf{F}}_{X_{ij}}^{\Psi} = \frac{1}{2} \Gamma(2 - \alpha(\mathbf{X})) Q_{ij} \left[\frac{L_{-j}^{\alpha(\mathbf{X}) - 1}}{\Gamma(1 - \alpha(\mathbf{X}))} \right]$$



$$\int_{X_{-j}}^{X_{j}} \frac{1}{(X_{j} - X'_{j})^{\alpha(X)}} dX'_{j} + \frac{L_{+j}^{\alpha(X) - 1}}{\Gamma(1 - \alpha(X))} \int_{X_{j}}^{X_{+j}} \frac{1}{(X'_{j} - X_{j})^{\alpha(X)}} dX'_{j} \right]$$
(38)

Since the exponent of the power-law kernel $\alpha(X)$ is independent of the integrating variable X', the above expression can be easily simplified (by treating X as a constant within the integration) as:

$$\tilde{\mathbf{F}}_{X_{ij}}^{\Psi} = \frac{1}{2} \left[L_{-j}^{\alpha(X)-1} (X_j - X_{-j})^{1-\alpha(X)} + L_{+j}^{\alpha(X)-1} (X_{+j} - X_j)^{1-\alpha(X)} \right] Q_{ij}$$
(39)

In the above simplifications we have used the following property of the $\Gamma(\cdot)$ function: $\Gamma(2-\alpha)=(1-\alpha)\Gamma(1-\alpha)$. As highlighted in §2, the length scales L_{-j} and L_{+j} are taken such that: $L_{-j}=X_j-X_{-j}$ and $L_{+j}=X_{+j}-X_j$. This has also been illustrated schematically in Fig. 1b. By substituting these relations in Eq. (39), it follows that $\tilde{\mathbf{F}}_X^\Psi=\mathbf{Q}$ at all times. We also emphasize that the nonlocal formulation allows for an exact treatment of frame invariance in the presence of asymmetric horizons which occur at points close to material boundaries and interfaces. The different horizon lengths L_{-j} and L_{+j} enables the truncation of the horizon at points close to or on the boundary in order to exactly satisfy frame-invariance.

Type-II derivative: We consider a general formulation involving the left- and right-handed type-II VO Caputo derivatives. More specifically, we replace the length scale factors introduced in Eq. (2) with general multiplying factors c_1 and c_2 , and then find expressions for c_1 and c_2 such that the resulting formulation is frame-invariant. Using the definition of the type-II VO Caputo derivatives from Eq. (32) it follows that:

$$\tilde{\mathbf{F}}_{X_{ij}}^{\Psi} = c_1 \int_{X_{-j}}^{X_j} \frac{1}{\Gamma(1 - \alpha(X'))} \left[\frac{D_{X'_j}^1 \Psi_i(X', t)}{(X_j - X'_j)^{\alpha(X')}} \right] dX'_j
+ c_2 \int_{X_j}^{X_{+j}} \frac{1}{\Gamma(1 - \alpha(X'))} \left[\frac{D_{X'_j}^1 \Psi_i(X', t)}{(X'_j - X_j)^{\alpha(X')}} \right] dX'_j$$
(40)

Retracing the steps in Eqs. (36,37), under the rigid body motion Ψ , we obtain:

$$\tilde{\mathbf{F}}_{X_{ij}}^{\Psi} = Q_{ij} \left[c_1 \int_{X_{-i}}^{X_j} \frac{(X_j - X'_j)^{-\alpha(X')}}{\Gamma(1 - \alpha(X'))} dX'_j \right]$$

$$+c_2 \int_{X_j}^{X_{+j}} \frac{(X_j' - X_j)^{-\alpha(X')}}{\Gamma(1 - \alpha(X'))} dX_j'$$
 (41)

For frame-invariance, it is necessary that $\tilde{\mathbf{F}}_{X_{ij}}^{\Psi} = Q_{ij}$ at all times and for all points within the nonlocal solid. More specifically, we obtain the following equation:

$$c_{1} \underbrace{\int_{X_{-j}}^{X_{j}} \frac{(X_{j} - X'_{j})^{-\alpha(X')}}{\Gamma(1 - \alpha(X'))} dX'_{j}}_{\text{Cannot be simplified further}} + c_{2} \underbrace{\int_{X_{j}}^{X_{+j}} \frac{(X'_{j} - X_{j})^{-\alpha(X')}}{\Gamma(1 - \alpha(X'))} dX'_{j}}_{\text{Canada a simplified for the simplified for$$

To ensure that the above relation holds true for all points X, at all time instants, and for every order distribution, it is essential to evaluate the integrals highlighted in the equation above. However, given the functional variation of the VO, it is not straightforward to analytically evaluate the integrals. In fact, the possibility to obtain an analytical expression of the solution depends on the specific functional variation of the fractional-order. For the specific cases, where the analytical solution does not exist, it might not be possible to achieve a frame-invariant formulation. While the integrals could certainly be numerically evaluated, the numerical route poses additional computational challenges. The latter comment stems from the fact that the values of the specific integrals highlighted above depend on the position X as well as the specific functional variation of the order. Further, contrary to the type-I case where these factors turn out as the dimensions of the horizon of nonlocality, no physical interpretation can be conclusively drawn for the factors when using type-II derivatives.

Type-III derivative: By using the definition of the type-III derivatives and the arguments presented for the type-II derivative, Eq. (41) can be modified for a formulation using type-III derivatives as:

$$\tilde{\mathbf{F}}_{X_{ij}}^{\Psi} = Q_{ij} \left[c_1 \underbrace{\int_{X_{-j}}^{X_j} \frac{(X_j - X_j')^{-\alpha(X - X')}}{\Gamma(1 - \alpha(X - X'))}}_{\text{Cannot be simplified further}} dX_j' \right] + c_2 \underbrace{\int_{X_j}^{X_{+j}} \frac{(X_j' - X_j)^{-\alpha(X - X')}}{\Gamma(1 - \alpha(X - X'))}}_{\text{Cannot be simplified further}} dX_j' \right]$$
(43)

Given the specific form of the VO, similar to type-II derivatives, it is not always possible to obtain a closed form expression for the factors c_1 and c_2 . It immediately follows that the remarks made above for type-II also hold true for type-III derivatives.

To summarize, the use of type-II and type-III VO derivatives is more likely to lead to non frame-invariant formulations. For cases, where a frame-invariant formulation can be achieved, the procedure to obtain the different factors is not general because frame-invariance must be re-valuated for every VO and at every point in the nonlocal solid. This makes the formulation computationally intensive and additionally, the obtained factors do not admit clear physical interpretations, unlike the length scale factors used in type-I derivatives.

C: Derivation of the governing equations

Theorem: The displacement field $u(x) \in \psi$, a class of all kinematically admissible displacement fields, which solves the Eqs. (7, 8) minimizes the total potential energy functional given in Eq. (6) in the class ψ . Conversely, the displacement field minimizing the total potential energy functional in Eq. (6) solves the fractional-order nonlocal beam governing Eqs. (7, 8).

Proof Let $u^* \in \psi$ be the unique solution to the system of Eqs. (7,8). Next, we assume $u = u^* + \delta u$ is another kinematically admissible field such that $\delta u \in \psi^*$. The class ψ^* is similar to the class ψ except for the boundary points $x \in \{0, L\}$, where the displacement degrees of freedom $\{u_0, w_0, D_x^1 w_0\} = 0$ in context of Eqs. (7,8). In the following, all quantities with the superscript \Box^* correspond to the displacement field u^* . Under the above conditions, following the principles of variational calculus, Eq. (6) can be expressed as:

$$\Pi[\boldsymbol{u}] = \Pi[\boldsymbol{u}^*] + \delta \Pi + \frac{1}{2} \delta^2 \Pi \tag{44}$$

where $\delta\Pi$ and $\delta^2\Pi$ are the first and second variations of Π from u^* . Using the Eqs. (5, 6, 9), the first variation $\delta\Pi$ is obtained as:

$$\delta\Pi = \underbrace{\int_{0}^{L} N_{xx}^{*} \left[D_{x}^{\alpha(x)} \delta u_{0} \right] dx}_{\mathcal{I}_{1}} - \underbrace{\int_{0}^{L} M_{xx}^{*} \left[D_{x}^{\alpha(x)} \left(D_{x}^{1} \delta w_{0} \right) \right] dx}_{\mathcal{I}_{2}}$$
$$- \int_{0}^{L} F_{a} \delta u_{0} dx - \int_{0}^{L} F_{t} \delta w_{0} dx \tag{45}$$

Simplification of \mathcal{I}_1 : We first simplify the term indicated as \mathcal{I}_1 . Using the definition of the VO-RC fractional derivative

 $\underline{\underline{\hat{\mathcal{D}}}}$ Springer

given in Eq. (2), we obtain:

$$\mathcal{I}_{1} = \frac{1}{2} \left[\underbrace{\int_{0}^{L} N_{xx}^{*} \left[l_{-}^{\alpha(x)-1} \Gamma(2 - \alpha(x))_{x-l_{-}}^{C} D_{x}^{\alpha(x)} \delta u_{0} \right] dx}_{\mathcal{I}_{11}} - \underbrace{\int_{0}^{L} N_{xx}^{*} \left[l_{+}^{\alpha(x)-1} \Gamma(2 - \alpha(x))_{x}^{C} D_{x+l_{+}}^{\alpha(x)} \delta u_{0} \right] dx}_{\mathcal{I}_{12}} \right]$$

$$(46)$$

From the definitions for the VO left- and right-handed Caputo derivatives given in Eq. (30) we obtain:

$$\mathcal{I}_{11} = \int_{0}^{L} N_{xx}^{*} l_{-}^{\alpha(x)-1} \frac{\Gamma(2-\alpha(x))}{\Gamma(1-\alpha(x))} \\
\left[\int_{x-l_{-}}^{x} (x-x')^{-\alpha(x)} \left(D_{x'}^{1} \delta u_{0} \right) dx' \right] dx \qquad (47a)$$

$$\mathcal{I}_{12} = -\int_{0}^{L} N_{xx}^{*} l_{+}^{\alpha(x)-1} \frac{\Gamma(2-\alpha(x))}{\Gamma(1-\alpha(x))} \\
\left[\int_{x}^{x+l_{+}} (x'-x)^{-\alpha(x)} \left(D_{x'}^{1} \delta u_{0} \right) dx' \right] dx \qquad (47b)$$

By changing the order of integration in the above equation, we obtain:

$$\mathcal{I}_{11} = \int_{0}^{L} D_{x'}^{1} \delta u_{0}$$

$$\left[\int_{x'}^{x'+l_{-}} l_{-}^{\alpha(x)-1} \frac{\Gamma(2-\alpha(x))}{\Gamma(1-\alpha(x))} \left(x - x' \right)^{-\alpha(x)} N_{xx}^{*} dx \right] dx'$$

$$(48a)$$

$$\mathcal{I}_{12} = -\int_{0}^{L} D_{x'}^{1} \delta u_{0}$$

$$\left[\int_{x'-l_{+}}^{x'} l_{+}^{\alpha(x)-1} \frac{\Gamma(2-\alpha(x))}{\Gamma(1-\alpha(x))} \left(x' - x \right)^{-\alpha(x)} N_{xx}^{*} dx \right] dx'$$

$$(48b)$$

Substituting the above expressions within Eq. (46) and using the definition of the VO Riesz integral given in Eq. (10), we obtain:

$$\mathcal{I}_{1} = \int_{0}^{L} \left[D_{x'}^{1} \delta u_{0} \right] \left[I_{x'}^{1-\alpha(x)} N_{xx}^{*} \right] dx'$$

$$\equiv \int_{0}^{L} \left[D_{x}^{1} \delta u_{0} \right] \left[I_{x}^{1-\alpha(x')} N_{xx}^{*} \right] dx \tag{49}$$

The above integrals are further evaluated using integration by parts in order to transfer the derivative from the independent the variable (axial displacement) to the secondary variable (stress resultant):

$$\mathcal{I}_{1} = \delta u_{0} \left[I_{x}^{1-\alpha(x')} N_{xx}^{*} \right] \Big|_{0}^{L} - \int_{0}^{L} \delta u_{0} D_{x}^{1} \left[I_{x}^{1-\alpha(x')} N_{xx}^{*} \right] dx$$
(50)

Now by using the definition of the VO R-RL derivative given in Eq. (11), we obtain:

$$\mathcal{I}_{1} = \delta u_{0} \left[I_{x}^{1-\alpha(x')} N_{xx}^{*} \right] \Big|_{0}^{L} - \int_{0}^{L} \delta u_{0} \left[\mathfrak{D}_{x}^{\alpha(x')} N_{xx}^{*} \right] dx \tag{51}$$

Simplification of \mathcal{I}_2 : By retracing the steps through Eqs. (46-51), it can be similarly shown that:

$$\mathcal{I}_{2} = \left(\delta D_{x}^{1} w_{0}\right) \left[I_{x}^{1-\alpha(x')} M_{xx}^{*}\right] \Big|_{0}^{L} - \delta w_{0} \left[\mathfrak{D}_{x}^{\alpha(x')} M_{xx}^{*}\right] \Big|_{0}^{L} + \int_{0}^{L} \delta w_{0} D_{x}^{1} \left[\mathfrak{D}_{x}^{\alpha(x')} N_{xx}^{*}\right] dx$$

$$(52)$$

Now by using the variational simplifications in Eqs. (45,51, 52) and the governing equations in Eq. (7,8) it can be shown that $\delta\Pi=0$. Additionally, the second variation $\delta^2\Pi$ is given as:

$$\delta^2 \Pi = \int_{\Omega} E_0 \delta[\varepsilon_{xx}] \delta[\varepsilon_{xx}] dV$$
 (53)

For any nontrivial $\delta u \in \psi^*$ we have from the above equation $\delta^2 \Pi > 0$, which leads us to the inequality:

$$\Pi[\boldsymbol{u}] = \Pi[\boldsymbol{u}^*] + \frac{1}{2}\delta^2 \Pi \ge \Pi[\boldsymbol{u}^*] \ \forall \ \boldsymbol{u} \in \psi$$
 (54)

It follows that the equality holds *iff* $u = u^* \forall x \in \Omega$. It follows immediately that, as claimed in the *Theorem* above, the displacement field u^* which solves the system of equations in Eqs. (7, 8) minimizes the functional Π in the class ψ .

Conversely, let u^* be the unique solution to the minimization problem: $\min(\Pi[u])$ such that $u \in \psi$. The minimization implies that for any variation $\delta u \in \psi^*$, $\delta \Pi$ evaluated at u^* must be identically zero. The $\delta \Pi$ is evaluated through Eqs. (45,51,52) where u^* , minimizes the functional Π . It follows that the stress field corresponding to the displacement field u^* uniquely satisfies the equilibrium Eqs. (7,8), and thus the set of fields $\{u^*, \varepsilon^*, \sigma^*\}$ solve the variable fractional-order Euler-Bernoulli beam equations.

References

 Hollkamp JP, Sen M, Semperlotti F (2018) Model-order reduction of lumped parameter systems via fractional calculus. J Sound Vib 419:526–543



- Hollkamp JP, Semperlotti F (2020) Application of fractional order operators to the simulation of ducts with acoustic black hole terminations. J Sound Vib 465:115035
- Bagley RL, Torvik PJ (1983) A theoretical basis for the application of fractional calculus to viscoelasticity. J Rheol 27:201–210
- Chatterjee A (2005) Statistical origins of fractional derivatives in viscoelasticity. J Sound Vib 284:1239–1245
- Benson DA, Schumer R, Meerschaert MM, Wheatcraft SW (2001)
 Fractional dispersion, Lévy motion, and the made tracer tests.
 Transp Porous Media 42:211–240
- Chen W, Holm S (2004) Fractional Laplacian time-space models for linear and nonlinear lossy media exhibiting arbitrary frequency power-law dependency. J Acoust Soc Am 115:1424–1430
- Holm S, Sinkus R (2010) A unifying fractional wave equation for compressional and shear waves. J Acoust Soc Am 127:542–548
- Buonocore S, Sen M, Semperlotti F (2019) Occurrence of anomalous diffusion and non-local response in highly-scattering acoustic periodic media. New J Phys 21:033011
- Buonocore S, Sen M (2020) Scattering cross sections of acoustic nonlocal inclusions: A fractional dynamic approach. J Appl Phys 127:203101
- Patnaik S, Semperlotti F (2020) A generalized fractional-order elastodynamic theory for non-local attenuating media. Proc R Soc A 476:20200200
- Patnaik S, Sidhardh S, Semperlotti F (2021) Displacement-driven approach to nonlocal elasticity. arXiv preprint arXiv:2104.05818
- Patnaik S, Sidhardh S, Semperlotti F (2020) A Ritz-based finite element method for a fractional-order boundary value problem of nonlocal elasticity. Int J Solids Struct 202:398–417
- Lazopoulos KA (2006) Non-local continuum mechanics and fractional calculus. Mech Res Commun 33:753–757
- Carpinteri A, Cornetti P, Sapora A (2014) Nonlocal elasticity: an approach based on fractional calculus. Meccanica 49:2551–2569
- Sumelka W, Blaszczyk T (2014) Fractional continua for linear elasticity. Archives Mech 66:147–172
- Alotta G, Failla G, Zingales M (2017) Finite-element formulation of a nonlocal hereditary fractional-order timoshenko beam. J Eng Mech 143:D4015001
- Sumelka W, Blaszczyk T, Liebold C (2015) Fractional Euler-Bernoulli beams: theory, numerical study and experimental validation. Eur J Mech-A/Solids 54:243–251
- Rahimi Z, Rezazadeh G, Sumelka W (2019) A non-local fractional stress-strain gradient theory. Int J Mech Mater Des 16:265–278
- Failla G, Santini A, Zingales M (2013) A non-local twodimensional foundation model. Arch Appl Mech 83:253–272
- Hollkamp JP, Sen M, Semperlotti F (2019) Analysis of dispersion and propagation properties in a periodic rod using a spacefractional wave equation. J Sound Vib 441:204–220
- Failla G, Zingales M (2020) Advanced materials modelling via fractional calculus: challenges and perspectives. Proc R Soc A 378:20200050
- Challamel N et al (2014) On nonconservativeness of Eringen's nonlocal elasticity in beam mechanics: correction from a discretebased approach. Archive Appl Mech 84:1275–1292
- Romano G, Barretta R, Diaco M, de Sciarra FM (2017) Constitutive boundary conditions and paradoxes in nonlocal elastic nanobeams. Int J Mech Sci 121:151–156
- Patnaik S, Sidhardh S, Semperlotti F (2021) Towards a unified approach to nonlocal elasticity via fractional-order mechanics. Int J Mech Sci 189:105992
- Glöckle WG, Nonnenmacher TF (1995) A fractional calculus approach to self-similar protein dynamics. Biophys J 68:46–53
- Meng R, Yin D, Drapaca CS (2019) Variable-order fractional description of compression deformation of amorphous glassy polymers. Comput Mech 64:163–171

- Meng R, Yin D, Drapaca CS (2019) A variable order fractional constitutive model of the viscoelastic behavior of polymers. Int J Non-Linear Mech 113:171–177
- Di Paola M, Alotta G, Burlon A, Failla G (2020) A novel approach to nonlinear variable-order fractional viscoelasticity. Phil Trans R Soc A 378:20190296
- Samko SG, Ross B (1993) Integration and differentiation to a variable fractional order. Integ Trans Spec Funct 1:277–300
- Lorenzo CF, Hartley TT (2002) Variable order and distributed order fractional operators. Nonlinear Dyn 29:57–98
- Coimbra C (2003) Mechanics with variable-order differential operators. Ann Phys 12:692–703
- Patnaik S, Semperlotti F (2020) Application of variable-and distributed-order fractional operators to the dynamic analysis of nonlinear oscillators. Nonlinear Dyn 100:561–580
- Patnaik S, Semperlotti F (2020) Modeling contacts and hysteretic behavior in discrete systems via variable-order fractional operators.
 J Comput Nonlinear Dyn 15
- Solís-Pérez J, Gómez-Aguilar J (2020) Variable-order fractalfractional time delay equations with power, exponential and Mittag-Leffler laws and their numerical solutions. Eng Comput 1–23
- 35. Chechkin AV, Gorenflo R, Sokolov IM (2005) Fractional diffusion in inhomogeneous media. J Phys A: Math Gen 38:L679
- Sun H, Chen W, Chen Y (2009) Variable-order fractional differential operators in anomalous diffusion modeling. Physica A 388:4586–4592
- Patnaik S, Hollkamp JP, Semperlotti F (2020) Applications of variable-order fractional operators: a review. Proc R Soc A 476:20190498
- 38. Patnaik S, Semperlotti F (2020) Variable-order particle dynamics: formulation and application to the simulation of edge dislocations. Phil Trans R Soc A 378:20190290
- Patnaik S, Semperlotti F (2021) Variable-order fracture mechanics and its application to dynamic fracture. npj Comput Mater 7:1–8
- Wu F, Liu JF, Wang J (2015) An improved Maxwell creep model for rock based on variable-order fractional derivatives. Environ Earth Sci 73:6965–6971
- Schuster M, Paliwal KK (1997) Bidirectional recurrent neural networks. IEEE Trans Signal Process 45:2673–2681
- Antil H, Otárola E, Salgado AJ (2018) Optimization with respect to order in a fractional diffusion model: analysis, approximation and algorithmic aspects. J Sci Comput 77:204

 –224
- D'Elia M, Gunzburger M (2016) Identification of the diffusion parameter in nonlocal steady diffusion problems. Appl Math Optim 73:227–249
- Salehinejad H, Sankar S, Barfett J, Colak E, Valaee S (2017) Recent advances in recurrent neural networks. arXiv preprint arXiv:1801.01078
- 45. Goodfellow I, Bengio Y, Courville A (2016) Deep learning. MIT Press, Cambridge
- Raissi M, Perdikaris P, Karniadakis GE (2019) Physics-informed neural networks: A deep learning framework for solving forward and inverse problems involving nonlinear partial differential equations. J Comput Phys 378:686–707
- 47. Mehta PP, Pang G, Song F, Karniadakis GE (2019) Discovering a universal variable-order fractional model for turbulent Couette flow using a physics-informed neural network. Fract Calculus Appl Anal 22:1675–1688
- Pang G, D'Elia M, Parks M, Karniadakis GE (2020) nPINNs: nonlocal physics-informed neural networks for a parametrized nonlocal universal Laplacian operator. algorithms and applications. J Comput Phys 422:109760
- Batra R (2021) Misuse of Eringen's nonlocal elasticity theory for functionally graded materials. Int J Eng Sci 159:103425



- Li Z, Wang H, Xiao R, Yang S (2017) A variable-order fractional differential equation model of shape memory polymers. Chaos Solitons Fractals 102:473–485
- Sun H, Chen W, Wei H, Chen Y (2011) A comparative study of constant-order and variable-order fractional models in characterizing memory property of systems. Eur Phys J Spec Top 193:185
- Szajek K, Sumelka W (2019) Discrete mass-spring structure identification in nonlocal continuum space-fractional model. Eur Phys J Plus 134:1–19
- Zhu H, Patnaik S, Walsh TF, Jared BH, Semperlotti F (2020) Nonlocal elastic metasurfaces: enabling broadband wave control via intentional nonlocality. Proc Natl Acad Sci 117:26099–26108
- Polizzotto C (2001) Nonlocal elasticity and related variational principles. Int J Solids Struct 38:7359–7380
- Wang CY, Murmu T, Adhikari S (2011) Mechanisms of nonlocal effect on the vibration of nanoplates. Appl Phys Lett 98:153101
- Capecchi D, Ruta G, Trovalusci P (2011) Voigt and Poincaré's mechanistic-energetic approaches to linear elasticity and suggestions for multiscale modelling. Archive Appl Mech 81:1573–1584
- Nair S (2019) Nonlocal Acoustic Black Hole Metastructures: Achieving Ultralow Frequency and Broadband Vibration Attenuation. Ph.D. thesis, Purdue University Graduate School
- Sainath TN, Vinyals O, Senior A, Sak H (2015) Convolutional, long short-term memory, fully connected deep neural networks.
 In: 2015 IEEE International Conference on Acoustics, Speech and Signal Processing (ICASSP), 4580–4584 (IEEE, 2015)
- Gers FA, Schmidhuber J, Cummins F (1999) Learning to forget: continual prediction with LSTM. In: IET conference proceedings, pp 850–855(5)
- Glorot X, Bengio Y (2010) Understanding the difficulty of training deep feedforward neural networks. In: Proceedings of the thirteenth international conference on artificial intelligence and statistics, pp. 249–256 (JMLR Workshop and Conference Proceedings, 2010)
- Kingma DP, Ba J (2014) Adam: a method for stochastic optimization. arXiv preprint arXiv:1412.6980
- Hossain MS, Ong ZC, Ismail Z, Noroozi S, Khoo SY (2017) Artificial neural networks for vibration based inverse parametric identifications: a review. Appl Soft Comput 52:203–219

- Yan L, Zhou T (2019) An adaptive surrogate modeling based on deep neural networks for large-scale Bayesian inverse problems. arXiv preprint arXiv:1911.08926
- Padmanabha GA, Zabaras N (2021) Solving inverse problems using conditional invertible neural networks. J Comput Phys 433:110194
- Lorensen WE, Cline HE (1987) Marching cubes: a high resolution 3D surface construction algorithm. ACM siggraph Comput Graph 21:163–169
- Szilvśi-Nagy M, Matyasi G (2003) Analysis of STL files. Math Comput Model 38:945–960
- Chen D, Yang J, Kitipornchai S (2015) Elastic buckling and static bending of shear deformable functionally graded porous beam. Compos Struct 133:54

 61
- 68. Anirudh B, Ganapathi M, Anant C, Polit O (2019) A comprehensive analysis of porous graphene-reinforced curved beams by finite element approach using higher-order structural theory: Bending, vibration and buckling. Compos Struct 222:110899
- Trovalusci P, De Bellis ML, Masiani R (2017) A multiscale description of particle composites: From lattice microstructures to micropolar continua. Compos B Eng 128:164–173
- Devarajan B, Kapania RK (2020) Thermal buckling of curvilinearly stiffened laminated composite plates with cutouts using isogeometric analysis. Compos Struct 238:111881
- Devarajan B (2021) Analyzing thermal buckling in curvilinearly stiffened composite plates with arbitrary shaped cutouts using isogeometric level set method. arXiv preprint arXiv:2104.05132
- Ortigueira MD, Valério D, Machado JT (2019) Variable order fractional systems. Commun Nonlinear Sci Numer Simul 71:231–243

Publisher's Note Springer Nature remains neutral with regard to jurisdictional claims in published maps and institutional affiliations.

